AFRL-RV-PS-
TP-2017-0025

3D REGIONAL WAVE PROPAGATION WITH Q(f) IN EAST ASIA
Annual Report

Kim B. Olsen

San Diego State University
GMCS 231A
5500 Campanile Dr.
San Diego, CA 92182

01 June 2017

Technical Report

APPROVED FOR PUBLIC RELEASE; DISTRIBUTION IS UNLIMITED.

AIR FORCE RESEARCH LABORATORY
Space Vehicles Directorate
3550 Aberdeen Ave SE
AIR FORCE MATERIEL COMMAND
KIRTLAND AIR FORCE BASE, NM 87117-5776

DTIC COPY

NOTICE AND SIGNATURE PAGE

Using Government drawings, specifications, or other data included in this document for any purpose other than Government procurement does not in any way obligate the U.S. Government. The fact that the Government formulated or supplied the drawings, specifications, or other data does not license the holder or any other person or corporation; or convey any rights or permission to manufacture, use, or sell any patented invention that may relate to them.

This report was cleared for public release by the AFMC/PA Office and is available to the general public, including foreign nationals. Copies may be obtained from the Defense Technical Information Center (DTIC) (http://www.dtic.mil).

AFRL-RV-PS-TP-2017-0025 HAS BEEN REVIEWED AND IS APPROVED FOR PUBLICATION IN ACCORDANCE WITH ASSIGNED DISTRIBUTION STATEMENT.

//SIGNED//	//SIGNED//
Dr. Frederick Schult Program Manager, AFRL/RVBYE	Dr. Thomas R. Caudill, Acting Chief AFRL Battlespace Environment Division

This report is published in the interest of scientific and technical information exchange, and its publication does not constitute the Government's approval or disapproval of its ideas or findings.

REPORT DOCUMENTATION PAGE

Form Approved
OMB No. 0704-0188

Public reporting burden for this collection of information is estimated to average 1 hour per response, including the time for reviewing instructions, searching existing data sources, gathering and maintaining the data needed, and completing and reviewing this collection of information. Send comments regarding this burden estimate or any other aspect of this collection of information, including suggestions for reducing this burden to Department of Defense, Washington Headquarters Services, Directorate for Information Operations and Reports (0704-0188), 1215 Jefferson Davis Highway, Suite 1204, Arlington, VA 22202-4302. Respondents should be aware that notwithstanding any other provision of law, no person shall be subject to any penalty for failing to comply with a collection of information if it does not display a currently valid OMB control number. **PLEASE DO NOT RETURN YOUR FORM TO THE ABOVE ADDRESS.**

1. REPORT DATE *(DD-MM-YYYY)*	**2. REPORT TYPE**	**3. DATES COVERED** *(From - To)*
01-06-2017	Technical Report	01 Jun 2016 – 01 Jun 2017

4. TITLE AND SUBTITLE
3D REGIONAL WAVE PROPAGATION WITH Q(f) IN EAST ASIA
Annual Report

5a. CONTRACT NUMBER
FA9453-16-C-0017

5b. GRANT NUMBER

5c. PROGRAM ELEMENT NUMBER
62601F

6. AUTHOR(S)
Kim B. Olsen

5d. PROJECT NUMBER
1010

5e. TASK NUMBER
PPM00019634

5f. WORK UNIT NUMBER
EF128702

7. PERFORMING ORGANIZATION NAME(S) AND ADDRESS(ES)
San Diego State University
GMCS 231A
5500 Campanile Dr.
San Diego, CA 92182

8. PERFORMING ORGANIZATION REPORT NUMBER

9. SPONSORING / MONITORING AGENCY NAME(S) AND ADDRESS(ES)
Air Force Research Laboratory
Space Vehicles Directorate
3550 Aberdeen Avenue SE
Kirtland AFB, NM 87117-5776

10. SPONSOR/MONITOR'S ACRONYM(S)
AFRL/RVBYE

11. SPONSOR/MONITOR'S REPORT NUMBER(S)
AFRL-RV-PS-TP-2017-0025

12. DISTRIBUTION / AVAILABILITY STATEMENT
Approved for public release; distribution is unlimited. (AFMC-2018-0041 dtd 22 May 2018)

13. SUPPLEMENTARY NOTES

14. ABSTRACT
This first annual report for FA9453-16-C-0017 provides a review of work accomplished, work in progress, and next steps. We collaborate with Scott Phillips and Mike Begnaud of LANL to use 3D high-performance computing to reproduce high-frequency (<4Hz) regional records (450km+) from the seismic sources at the North Korea nuclear test site (NKNTS). The project constrains the crustal parameters, in terms of seismic velocities, densities, frequency-dependent anelastic attenuation, and distributions of small-scale heterogeneities, required to match the observed records. The results help understand the nature of crustal scattering on the Korean Peninsula, and have implications for methods used for discrimination between explosive and earthquake sources.

15. SUBJECT TERMS
finite differences, numerical modeling, high-performance computing, discrimination, high-frequency deterministic modeling, North Korea nuclear tests, frequency-dependent Q, statistical distributions of small-scale heterogeneities

16. SECURITY CLASSIFICATION OF:			**17. LIMITATION OF ABSTRACT**	**18. NUMBER OF PAGES**	**19a. NAME OF RESPONSIBLE PERSON**
a. REPORT	**b. ABSTRACT**	**c. THIS PAGE**			Dr. Frederick Schult
Unclassified	Unclassified	Unclassified	Unlimited	50	**19b. TELEPHONE NUMBER** *(include area code)*

This page is intentionally left blank.

Approved for public release; distribution is unlimited.

Table of Contents

List of Figures

1. SUMMARY

We have carried out 3D finite difference simulations (FD, <4 Hz) of regional wave propagation for the 2009 North Korea nuclear explosion and compared to instrument-corrected records at stations INCN and TJN in South Korea. The source is an isotropic explosion with a moment magnitude of 4.1. Synthetics computed in the relatively smooth Sandia/Los Alamos National Laboratory SALSA3D velocity model significantly overpredict Rayleigh wave amplitudes by more than an order of magnitude while underpredicting coda amplitudes. The addition to SALSA3D of a von Karman distribution of small-scale heterogeneities with correlation lengths of ~1,000 m, Hurst number of 0.1, and horizontal-to-vertical anisotropy of ~5 produces synthetics in general agreement with the data. The best fits are obtained from models with gradient in the strength of the velocity and density perturbations, and strong scattering (10%) limited to the top 7.5-10 km of the crust. Deeper scattering tends to decrease the initial P wave amplitudes to levels much below those for the data, a critical result for methods discriminating between explosive and earthquake sources. In particular, the amplitude at the onset of P_n can be affected by as little as 2% small-scale heterogeneity in the lower crust and upper mantle. Simulations including constant Q of 200-300 below 1 Hz and a power-law Q(f) formulation at higher frequencies with an exponent of 0.3 (P and S-waves) generate synthetics in best agreement with the data. Our results suggest that very limited scattering contributions from the near-source area accumulates along the regional path.

2. INTRODUCTION

The primary aim of nuclear explosion monitoring is to be able to detect nuclear explosions, which includes discrimination between seismic records generated by different sources. The seismic signature in the records used in explosion monitoring is a combination of source, path and local site effects. The origin of the source generally provides a constraint on the relative amount of P, S and surface wave phases included in the recorded waves. While explosive sources typically give rise to records with a relatively large ratio of P-to-S waves, details of such trends depend on the length and character of the crustal path encountered by the waves.

In many cases, the closest available records are obtained from stations several hundred kilometers from the source, typically causing the addition of severe path effects to the recorded seismic waves. These path effects are generated by a combination of (frequency-dependent) anelastic attenuation, crustal scattering, focusing, and multi-pathing. Unless detailed modeling can be carried out to sufficiently high frequencies, path effects can lead to misinterpretation of the origin of the wave trains. It is therefore imperative to be able to replicate the general characteristics of the seismic records from regional wave propagation.

Conventionally, regional modeling of crustal wave propagation has been carried out using either 1D or 2D approximations due to the large computational cost associated with fully 3D deterministic models. However, recent advances in available supercomputing resources has facilitated full-waveform simulations in 3D velocity models for frequencies up to several Hertz. For example, Takemura et al. (2015)

simulated wave propagation out to distances of about 70 km from explosive and earthquake sources for frequencies up to 4.2 Hz in Japan. Rodgers et al. (2010) investigated topographic scattering effects and Pitarka et al. (2015) simulated the seismic signature of a chemical explosion in 3D crustal models using FD methods.

Accurate ground modeling requires that anelastic attenuation, typically parameterized by Q, be included. For frequencies less than about 1 Hz, a frequency-independent Q approach has generally been sufficient to fit the distance decay of seismic amplitudes caused by anelastic losses (e.g., Olsen, 2000; Cui et al., 2010; and many other studies). However, as frequencies increase, seismic data demands frequency dependency of Q, with progressively decreasing attenuation (e.g., Raoof et al., 1999; Lekic et al., 2009; McNamara et al., 2012; Phillips et al., 2013). Such frequency-dependency of Q can be formulated numerically for deterministic ground motion simulations (Withers et al., 2015). Moreover, as frequencies grow, small-scale heterogeneities of the medium increasingly affect the wave propagation via scattering. While not feasible to directly map the in-situ small-scale crustal variation, the velocity and density perturbations can be formulated statistically. Using such techniques, several studies have proposed ranges of the controlling parameters from analyses of sonic logs and V_s30 data (e.g., Savran and Olsen, 2016) and ambient noise modeling (Nakata and Beroza, 2015).

The primary objective of this study is to push the simulation of wave propagation in state-of-the-art 3D crustal models from shallow explosive sources to larger distances and higher frequencies using validation from broadband seismic data. We have reached a point where High Performance Computing (HPC) capabilities and sophistication of scientific models allow simulating high-frequency (here, up to 4 Hz) regional wave propagation to distances of several hundred kilometers. Our approach includes a highly-scalable FD method, a 3D crustal structure, Q(f), and statistical descriptions of small-scale velocity and density perturbations. First, we describe the velocity and Q(f) models used in the wave propagation. Then, the source and associated parameters used for the 2009 North Korea nuclear test are described, followed by a description of the seismic data used to constrain the model parameters at stations INCN and TJN in South Korea. We show ground motion synthetics compared to data at the two stations in the SALSA3D model, without and with various distributions of small-scale heterogeneities, exploring their depth dependency, strength, horizontal-to-vertical anisotropy, and proximity to the source. For clarity, we show results for station INCN in the main article, and leave the results at TJN for the Appendix.

3. METHODS, ASSUMPTIONS, AND PROCEDURES

3.1 Numerical Method

We have used the AWP-ODC-GPU code to simulate the wave propagation presented in this study. AWP-ODC-GPU is a highly-scalable GPU-based anelastic wave propagation code that solves the 3D velocity-stress wave equation explicitly by a staggered-grid FD method with fourth-order accuracy in space and second-order accuracy

in time (Olsen, 1994; Cui et al., 2013). The code has been extensively validated for a wide range of problems in 3D crustal models (e.g., Day et al., 2008; Bielak et al., 2010).

Anelastic attenuation plays a critical role for the regional propagation distances considered here. A power-law description of the form $Q=Q_o(f/f_o)^{\gamma}$ has been successfully used to model Q to higher frequencies, where Q_o and γ are region-dependent parameters. Here, we use the accurate coarse-grain memory-variable approach implemented in AWP-ODC by Withers et al., 2015, with separate values of Q for P-waves (Q_p) and S-waves (Q_s) specified for each grid point in the model.

3.2 Velocity Model

We have used velocity information from the SALSA3D (SAndia LoS Alamos 3D, Begnaud et al., 2012) global three-dimensional tomography model of the Earth's crust and mantle. The model was developed to obtain improved locations of explosive sources, with P- and S-wave velocity distributions obtained by separate tomographic inversions. Density in our calculations was calculated from V_s using the relation by Nafe and Drake (1957) for V_p<6.2 km/s, and Birch's law (Birch, 1961) for V_p>6.2, with a smooth transition between the two regions.

Figure 1 shows the distribution of V_s at a depth of 3.3 km in the region used to model the wave propagation from the North Korea nuclear test site (NKNTS), a 450 km (E-W) by 670 km (N-S) by 80 km (depth) sub-volume of the SALSA3D model at a uniform grid spacing of 100 m everywhere (24 billion grid points). Note the higher velocities inside the N-S oriented band within the Korean peninsula, as compared to the continental shelf to the east. It is clear that SALSA3D in our area of interest is considerably smooth, with apparent horizontal correlation lengths on the order of tens to hundreds of kilometers. This lack of smaller-scale variation is addressed separately through a statistical approach, in order to introduce realistic scattering for frequencies up to 4 Hz (see section **Introducing Small-scale Media Heterogeneities**).

3.3 Source Description

We modeled the source for the 2009 NKNTS at 41.2914^o North, 129.0819^o East, at a depth of 600 m below the surface, consistent with the location found by Patton and Pabian (2014). Ford et al. (2009) and Shin et al. (2010) estimated a total M_w for the event of ~4.5. However, Ford et al. (2009) also found that the isotropic component of the source provided fits the data almost as well as the full solution. In our model the source is therefore defined as an isotropic, purely explosive point source with a moment magnitude of 4.1 (moment 1.58e^{15} Nm) based on the results by Ford et al (2009) and Shin et al. (2010). Figure A1 shows details of the simulated source function.

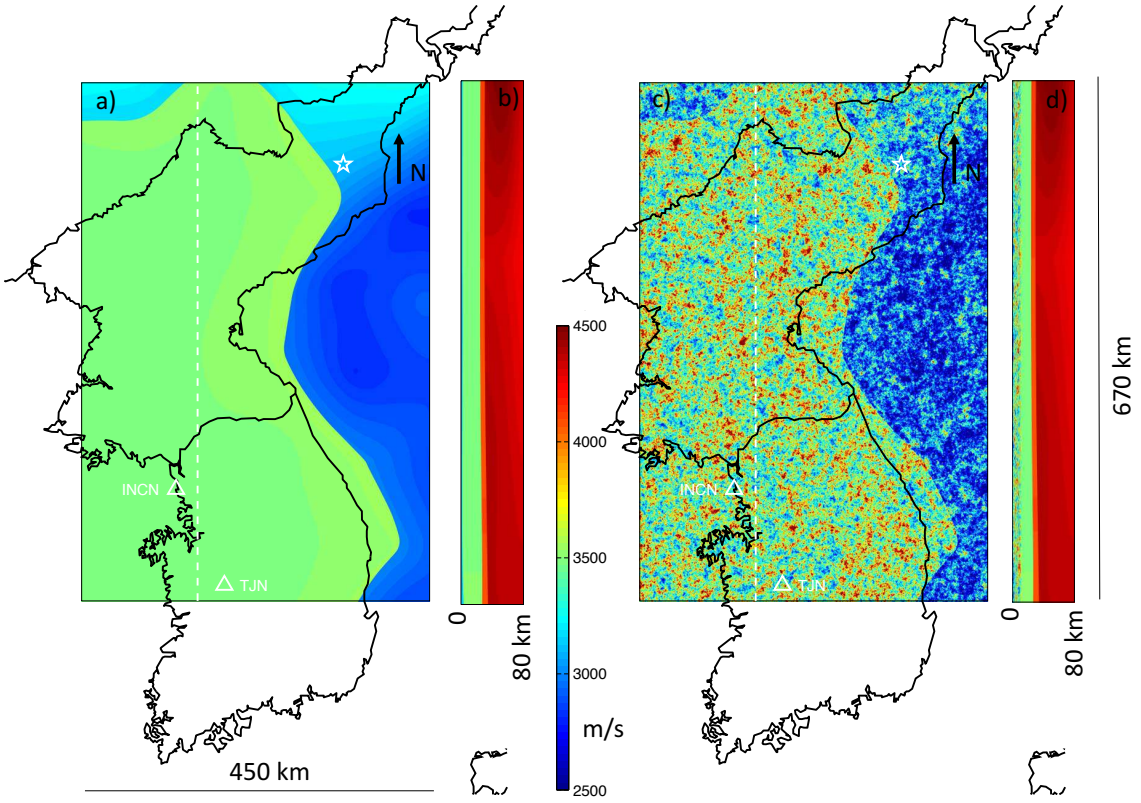

Figure 1. S-wave velocity from the SALSA3D model at 3.3 km depth (a) without (Model 1 in Table 1) and (c) with a distribution of small-scale heterogeneities (a=1000 m, υ=0.1, σ=10%, H/V=5, Model 6 in Table 1). ***Cross-sections along the N-S profile denoted by the dashed white line are shown next to the depth sections (b, d). The star denotes the source location for the May 25 2009 North Korea nuclear test. Two stations (INCN, TJN) in South Korea with instrument-corrected records available used in this study are shown by white triangles.***

3.4 Seismic Data Constraints

We use instrument-response corrected ground motion histories from stations INCN and TJN (see Figure 1 for station locations). Data from additional stations in South Korea exist (see, e.g., Shin et al., 2010) but were not accessible for our study. The data were low-pass filtered to 4 Hz with a 10-pole Butterworth filter with two forward passes and the horizontal components were rotated into radial and transverse components. For the waveform comparisons presented in this study we repeated this processing procedure for the synthetics.

3.5 Regional Wave Propagation

Several studies have reported values for Q in east Asia, typically crustal-wide estimates associated with specific phases such as P_n, P_g, S_n and L_g waves, including Mitchel et al., 1997; Xie et al., 2006; Hong and Rhie, 2009; and Ford et al., 2010. These

studies typically report crustal-wide values of Q_o and γ assuming a power-law relation $Q=Q_o(f/f_o)^{\gamma}$, obtained from attenuation tomography methods. In general, these results tend to agree reasonably well for the Korean Peninsula. These studies typically report Q values associated with phases such as P_n, P_g, S_n and L_g. It is not immediately clear how these Q values relate to those for P- and S-waves, which are required for the viscoelastic modeling with AWP-ODC. As a starting point for our modeling, we select values of $Q_{os}=Q_{op}=350$ and $\gamma=0.3$ as a reference model for our simulations (Model 1, see Table 1), based on the published studies listed above.

Figure 2 shows three-component snapshots of velocity wave propagation in Model 1. The snapshots show coherent P and surface waves developing at the NKNTS at 27.5 s, with some limited P-S scattered energy developing in between. At 82.5 s the amplitudes of the P waves have diminished to a level not observable relative to that for the coherent surface waves at 82.5 s and later times. The surface waves impinge on South Korea around 137.5 s, and propagate between stations INCN and TJN at 192.5 s. The largest surface wave amplitudes are found on the vertical component, consistent with the particle motion of a Rayleigh wave. The surface waves are slowed down in the offshore area east of the Korean Peninsula due to lower seismic velocities.

Comparisons of observed and simulated 0-4 Hz waveforms in the SALSA3D model for the 2009 NKNTS at INCN and TJN are shown in Figures 3 and A2, respectively. In these figures, and subsequent waveform comparisons, we identify the expected arrival times for P_n as 7.0s + dist/vg(P_n), P_g as dist/vg(P_g), S_n as 12.0s + dist/vg(S_n), and L_g as dist/vg(L_g), where dist is the horizontal distance between the source and station, and vg is the group velocity of the particular phase. We use group velocity ranges of 7.6-8.2 km/s for P_n, 5.2-6.2 km/s for P_g, 4.0-4.7 km/s for S_n, and 3.0-3.6 km/s for L_g to define windows for the phases.

The radial and vertical components show large-amplitude initial P_n and P_g waves, and a strongly dispersive Rayleigh wave starting at the end of the L_g window, and persisting ~25 s past the window. The transverse component has little initial S-wave energy, but a dispersive Love wave appears simultaneously with the Rayleigh wave. It is evident from the comparison that the reference model very poorly reproduces the data from the two stations, in both time and frequency domains. Specifically, we observe the following areas in need of improvement: i) while initial (P) phases in the synthetics arrive at approximately at the expected time, their peak amplitudes are too large, ii) the surface waves are too energetic and arrive too late, iii) the amplitudes between the P wave and surface waves are too small, and iv) the spectral amplitudes are overpredicted for frequencies higher than about 0.4 Hz.

The details of the misfits in Figures 3 and A2 suggest that our reference model is deficient in scattering by smaller-scale features, not included in the rather smooth SALSA3D model. Scattering by geological features with scale lengths less than ~10 km, insufficiently represented in the model, is expected to introduce incoherency in and therefore decrease the amplitude of the P and surface waves, as well as generate converted body waves between the P and surface wave arrivals, and increase the late coda wave train. In order to improve the waveform fits we will introduce small-scale scattering in the SALSA3D model using a statistical approach.

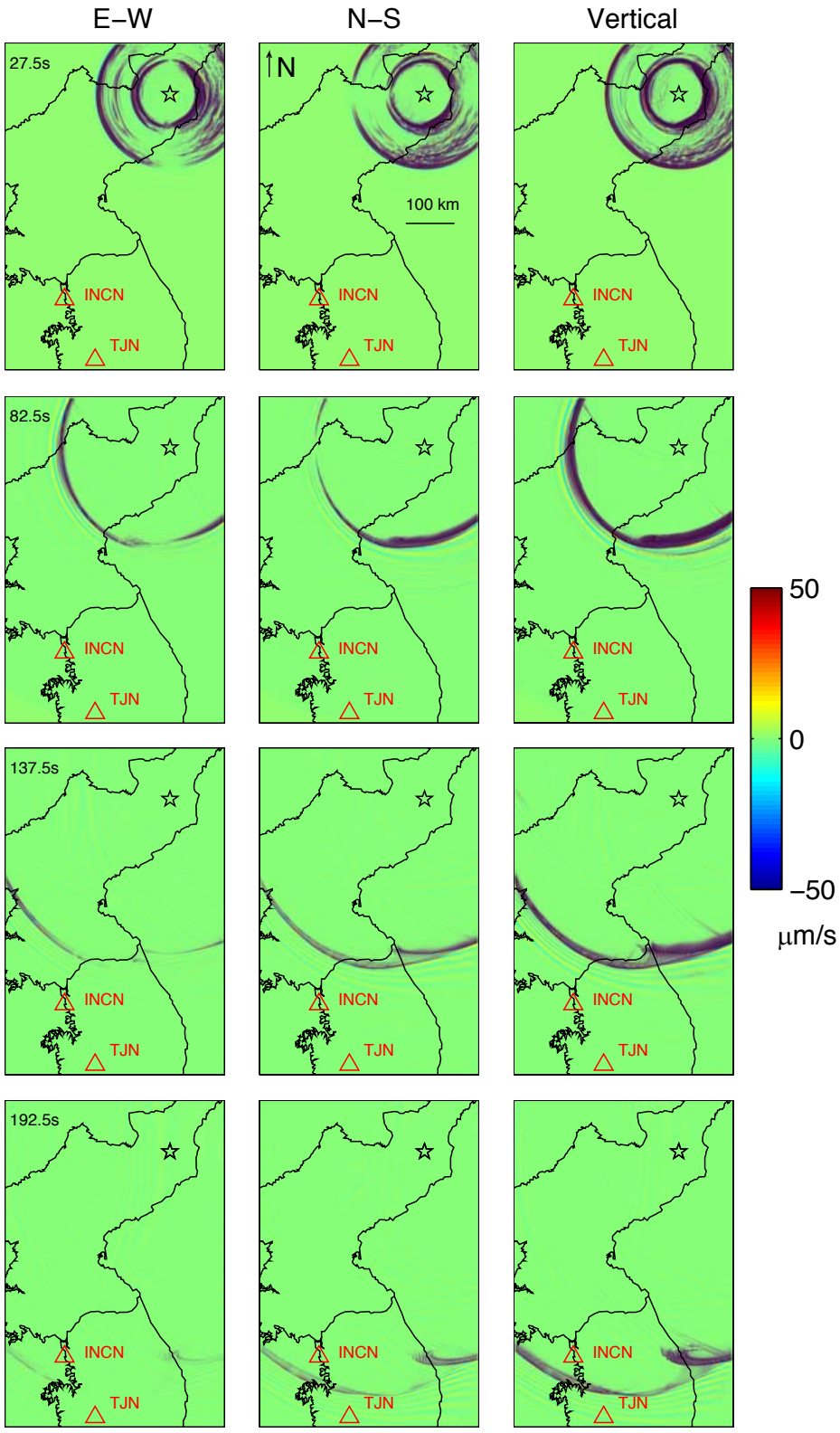

Figure 2. Snapshots of wave propagation (< 4 Hz) in SALSA3D (Model 1, Table 1).

Table 1. Q(f) and Small-scale Heterogeneity Parameters for FD Models*

Model	a (m)	R (km)	σ (%) $d<d_1$	d_1(km)	σ (%) $d>d_2$	d_2(km)	H/V	Seed	Q_o	γ
1	-	-	-	-	-	-	-	-	350	0.3
2	1,000	5	5	-	5	-	5	1	350	0.3
3	1,000	5	10	-	10	-	5	1	350	0.3
4	150	5	10	-	10	-	5	1	350	0.3
5	1,000	5	10	-	10	-	5	1	200	0.3
6	1,000	5	10	10	2	12.5	5	1	200	0.3
6a	1,000	0	10	10	0	12.5	5	1	200	0.3
7	1,000	0	10	7.5	2	10	5	1	200	0.3
7a	1,000	0	10	7.5	0	10	5	1	200	0.3
8	1,000	5	10	5	2	5	5	1	200	0.3
9	1,000	5	10	2.5	2	2.5	5	1	200	0.3
10	1,000	5	10	10	2	12.5	1	1	200	0.3
11	1,000	5	10	10	2	12.5	7	1	200	0.3
12	1,000	5	10	10	2	12.5	10	1	200	0.3
13	150	0	10	10	0	12.5	5	1	200	0.3
14	2,000	0	10	10	0	12.5	5	1	200	0.3
15	3,000	0	10	10	0	12.5	5	1	200	0.3
16	1,000	0.5	10	10	0	12.5	5	1	200	0.3
17	1,000	0.5	10	10	0	12.5	5	2	200	0.3
18	1,000	0.5	10	10	0	12.5	5	4	200	0.3
19	1,000	0.5	10	10	0	12.5	5	5	200	0.3
20	1,000	0.5	10	10	0	12.5	5	6	200	0.3

*All models use ν=0.1

a)

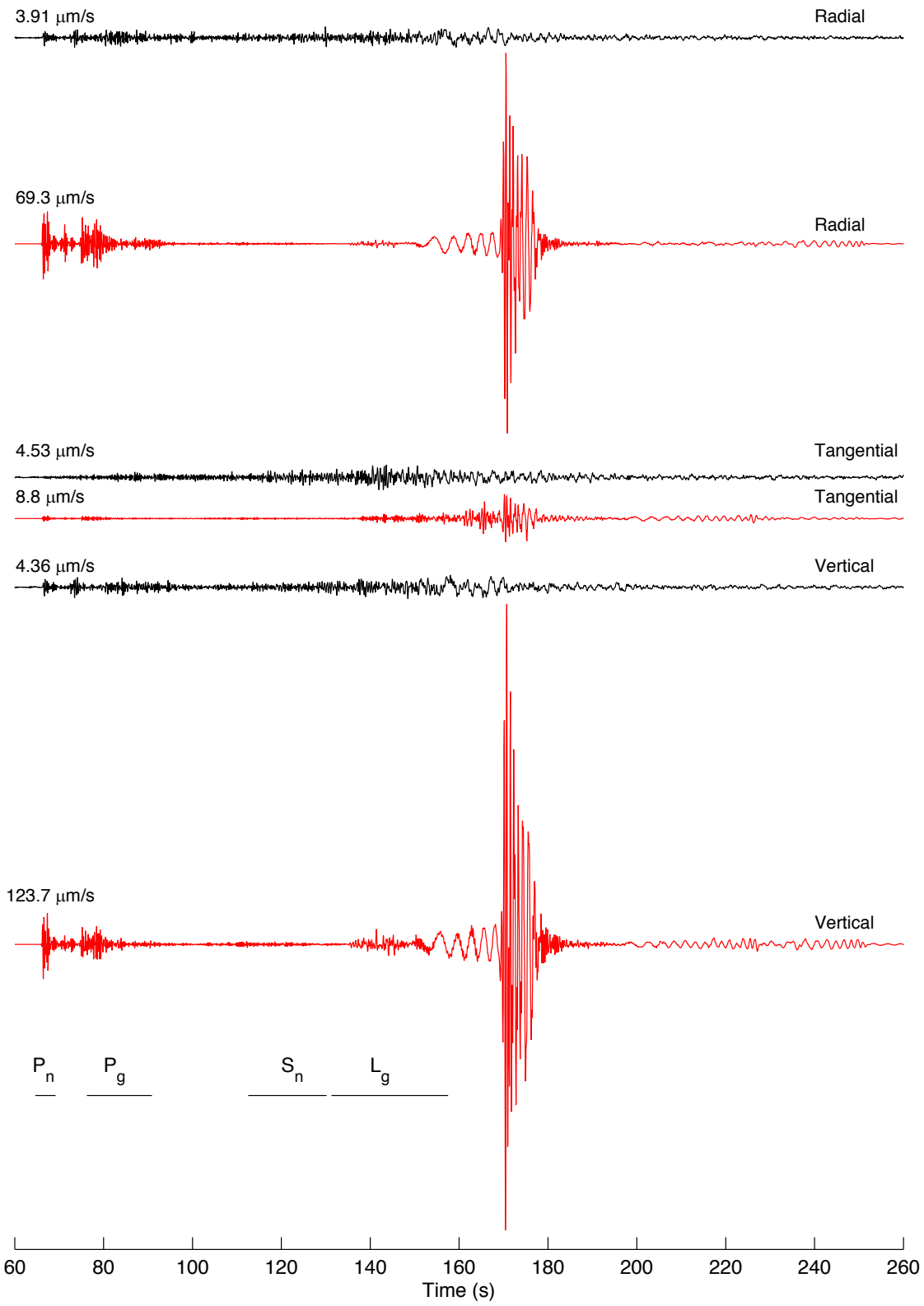

Figure 3. Comparison of observed (black) and synthetic waveforms at INCN using the SALSA3D model with small-scale heterogeneity Model 1 (Table 1) in (a) time and (b) frequency domains.

b)

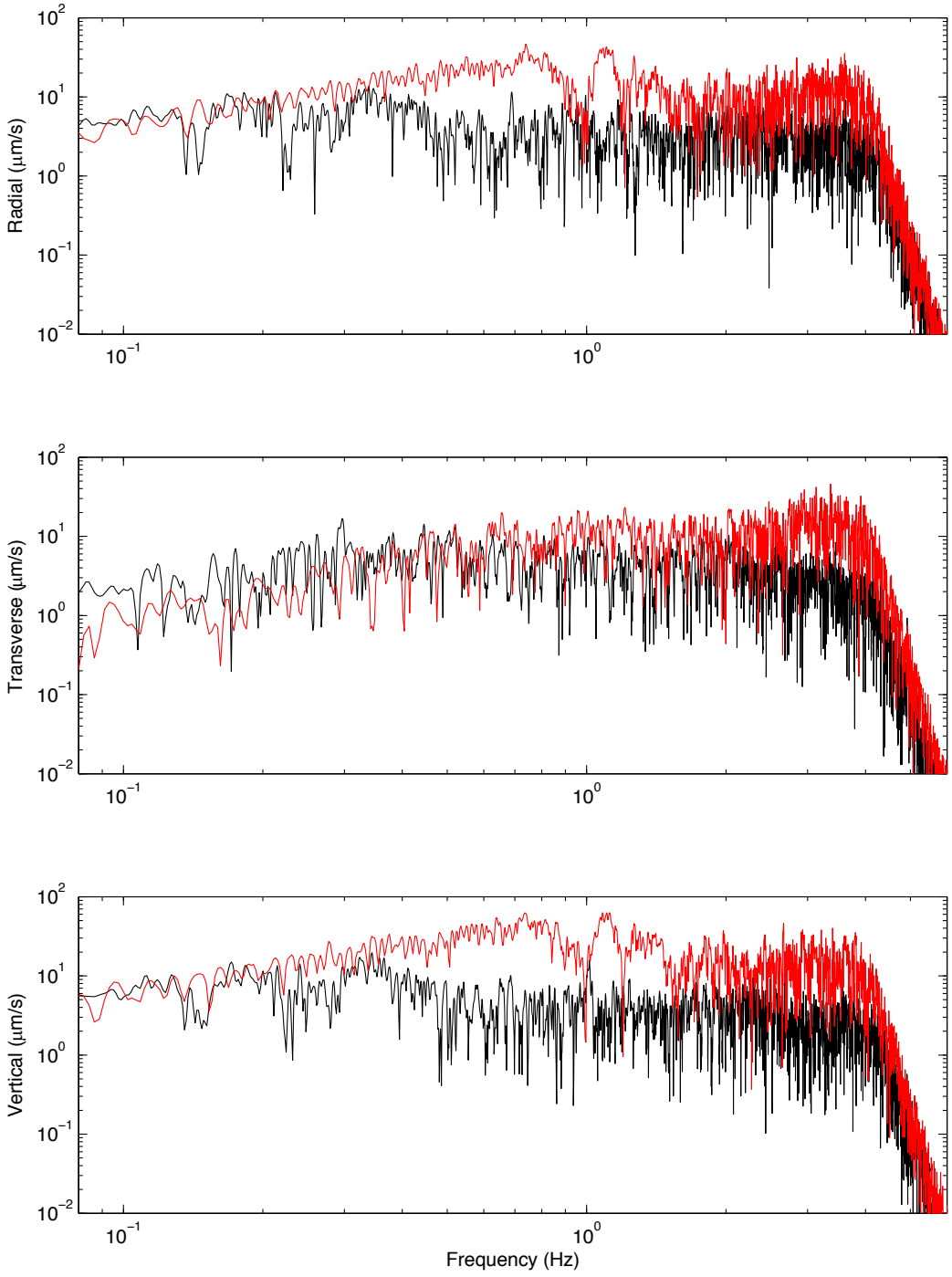

Figure 3 (continued). Comparison of observed (black) and synthetic waveforms at INCN using the SALSA3D model with small-scale heterogeneity Model 1 (Table 1) in (a) time and (b) frequency domains.

3.6 Small-Scale Media Heterogeneities

3.6.1 Statistical Description.

Small-scale heterogeneities can be described statistically, for example using von Karman auto covariance functions shown in eq. 1 with Fourier transform in eq. 2

$$\Phi_{\nu,L}(r) = \sigma^2 \frac{2^{1-\nu}}{\Gamma(\nu)} \left(\frac{r}{a}\right)^{\nu} K_{\nu}\left(\frac{r}{a}\right) \tag{1}$$

$$P(k) = \frac{\sigma^2 (2\sqrt{\pi}a)^E \Gamma(\nu + E/2)}{\Gamma(\nu)(1 + k^2 a^2)^{\nu + E/2}}, \tag{2}$$

(Tatarski, 1961), or using other statistical descriptions (e.g., Gaussian or Exponential distributions, see for example, Frankel and Clayton, 1986). Constraints on the parameters of the statistical distributions - the correlation length, *a,* Hurst exponent, ν, and standard deviation, σ - can be obtained from sonic logs, digitized geological maps and V_s30 measurements (e.g., Levander, 1992; Wu et al., 1994; Levander et al., 1994; De et al., 1994; Holliger, 1992; Holliger, 1996; Holliger, 1997; Dolan et al., 1998; Plesch et al., 2014; Nakata and Beroza, 2015; Savran and Olsen, 2016). These studies report Hurst exponents of 0.0-0.3 and correlation lengths between 60-160 m in the vertical direction, and horizontal to vertical anisotropy (H/V) between ~2-25. There is considerable variation in the correlation lengths found among the studies, reflecting the variable constraints from the underlying data (e.g., teleseismics may favor longer correlation lengths as compared to data from near-field stations). Moreover, the results from analysis of detailed sonic logs with sample spacings < 1 m are prone to produce smaller (high frequency) values than those from much more coarsely distributed measurements (such as V_s30).

Other constraints on the parameters of the small-scale heterogeneities are obtained from applying the statistical distributions in wave propagation simulations. Frankel and Clayton (1986) generated small-scale heterogeneities with three distinct autocorrelation functions, Gaussian, exponential (corresponding to ν = 0.5), and self-similar (corresponding to a ν = 0.0). By testing end-member cases of the von Karman autocorrelation function their 2D simulations provided constraints on ν estimates for the small-scale heterogeneities that fall in the range [0.0, 0.5] with a preferred value of 0.0. Hartzell et al. (2010) used ν=0.0 with *a*=5-10 km and σ=5-10%, while Jacobsen and Olsen (2011) included statistical distributions with ν=[0.5-0.5], *a*=250 m and σ=5-10% in their simulations. Imperatori and Mai (2013) used a Hurst exponent of 0.3 with correlation lengths on the order of hundreds of meters to kilometers.

Using a von Karman model we have generated distributions of small-scale heterogeneities with parameters based on the published studies discussed above, and

added the result to the SALSA3D model. Figure 1 (right) shows horizontal and vertical slices of V_s, where *a*=1000 m, ν=0.1, σ=10%, H/V=5 (Model 2, see Table 1). In the following we use trial-and-error modeling to constrain the parameters of the statistical parameters of the von Karman and anelastic parameters generating synthetics with the best fit to data. In the series of tests concerning a particular parameter, all other parameters are kept constant.

3.6.2 Scattering Effects from Depth-independent Models.

Figures 4 (INCN) and A3 (TJN) show a comparison of data and simulations including a von Karman model with models 2-5, see Table 1. The small-scale heterogeneities are added to the entire depth extent of the reference model, and we use γ=0.3 for the frequency-dependent power-law exponent. Compared to Model 1 without small-scale heterogeneities, Model 2 with σ = 5% and Q_o=350 still produces a coherent Rayleigh wave, albeit with reduced amplitude, and the amplitudes between the P wave and surface waves and coda following the surface waves continue to be larger than that for the data. When σ is increased to 10% throughout the model (Model 3), the surface wave amplitudes are further reduced, the amplitudes between the P wave and surface waves are now similar to or smaller than those for the data, and the coda amplitude after the surface waves is increased from the 5% case (Model 2). Model 3 generates synthetics with coda amplitudes similar to data at TJN, but tends to overpredict those at INCN.

The Hurst number of the small-scale heterogeneities in models 2-5 (ν=0.1) was selected in agreement with the variogram analysis of borehole sonic logs from the Los Angeles basin (Savran and Olsen, 2016). This analysis also found vertical correlation logs of 50-150 m, much shorter than the a=1,000 m used in Models 2-3. However, it is clear from Model 4, using a=150m and σ =10%, that the shorter correlation length, while reducing the higher-frequency amplitudes in the synthetics, still produces Rayleigh Wave amplitudes much larger than those in the data. Thus, varying the parameters of the small-scale heterogeneities does not appear to produce a satisfactory fit of the synthetics to the data. Instead, a lower Q_o of 200 with a=1,000 m and σ =10% (Model 5) produces synthetics with closer match to the data at INCN, but generally underpredicting the data at TJN. This result suggests that the path from the NKNTS to TJN is characterized by somewhat smaller low-frequency attenuation (Q_o~350) than that to INCN (Q_o~200).

Probably the most pronounced effect of Models 2-5 on the synthetics is the reduction of the P_n amplitude to values much below those for the data. We examine in the following section whether this issue can be overcome using a depth dependency of σ.

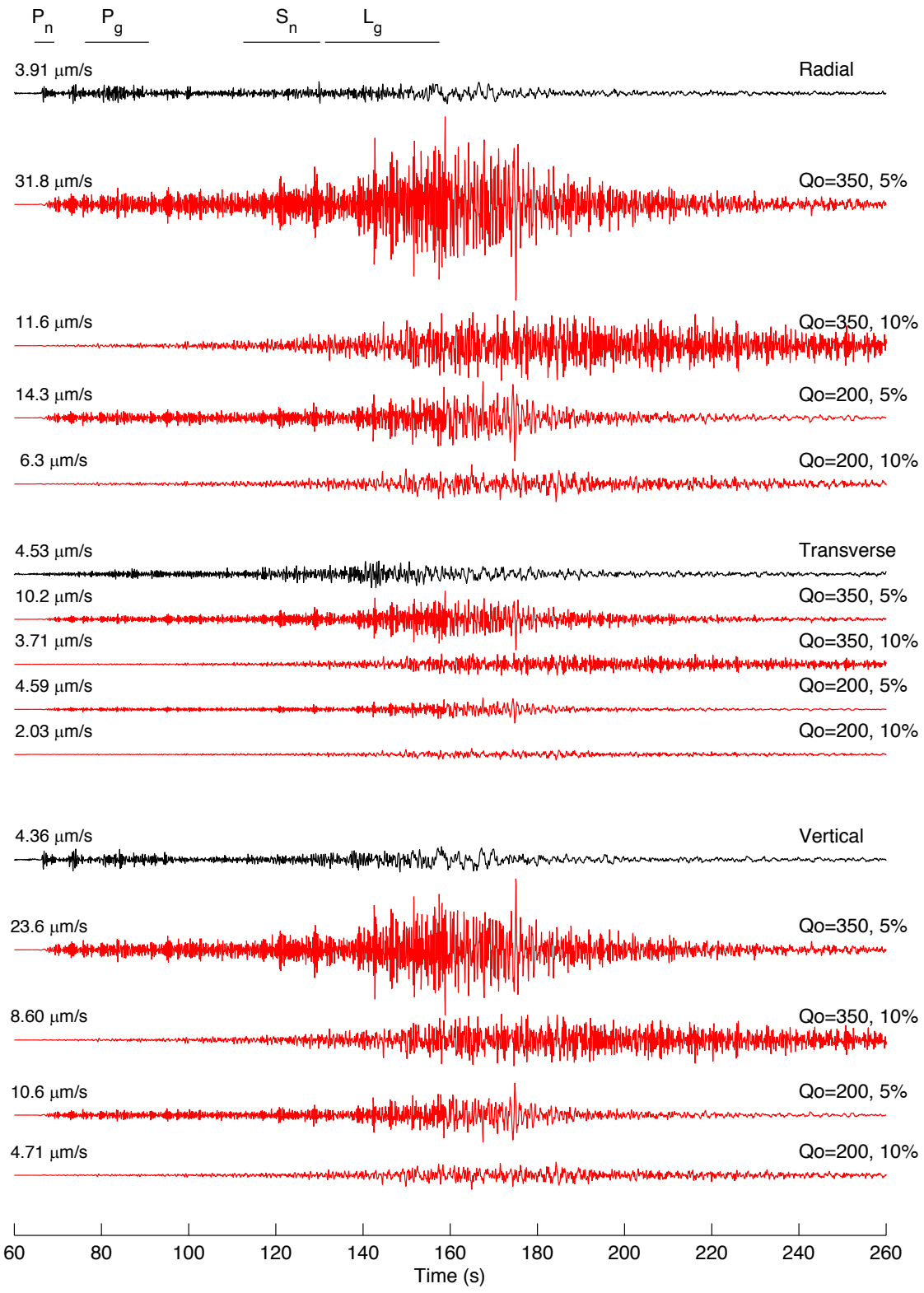

Figure 4. Comparison of observed (black) and synthetic waveforms at INCN for the SALSA3D model with Models 2-5 (Table 1).

3.6.3 Scattering Effects from Depth-dependent Models.

It is likely that the strength of the small-scale heterogeneities decreases with depth, for example due to the associated increase in lithostatic pressure and ductility of crustal material at deeper depths. To test such depth dependency of the scattering we have simulated wave propagation in 4 different gradient models of von Karman statistical distributions of small-scale heterogeneities (Figures 5, INCN, and A4, TJN, Models 6-9 in Table 1). The gradient models are all characterized by σ = 10% from the surface to a depth of d_1 (km), σ = 2% below a depth of d_2 (km), and a linear gradient in between. The values of d_1 and d_2 are listed by the synthetics. Here, we choose to use the relation $Q(f)=200\ f^{0.3}$ which produced an optimal fit for INCN using Model 5.

It is clear from Figs. 5 and A4 that the decrease in strength of the small-scale heterogeneities with depth in the upper crust improves the fit between the data and synthetics by generating larger amplitude initial P waves, and improving the amplitude of converted phases between the P and surface arrivals. Models 6-7 are selected for further analysis in the following sections based on their favorable fit to the data.

The scattering originating from the deeper parts of the model is further illustrated in Figs. 6 (INCN) and A5 (TJN), where the effects of the scattering from models with σ = 0% and 2% below the lower threshold depth (d_2) in the gradient models of Figs. 5 and A4 are highlighted. The results show that even a small value of σ of 2% below d_2 can have a significant effect on the wave train, including the first arriving P phases. Specifically, the gradient model with σ = 2% generates a gradual onset of P_n over 1-2 seconds, affecting the initial amplitude. On the other hand, if small-scale heterogeneities are omitted below d_2, the arrival time and amplitude of the P_n amplitudes are more impulsive. This result can have implications for techniques discriminating between explosive and earthquake sources based on ratios of P and S wave amplitudes. The modeling effects of the small-scale heterogeneities thus suggest that the scattering strength in the Earth's lower crust and the upper mantle strongly controls the amplitude and character of the initial P waves.

3.6.4 Constraints on Anisotropy of the Small-scale Crustal and Mantle Heterogeneities.

Several studies have estimated the horizontal-to-vertical anisotropy (H/V) of the small-scale heterogeneities in the crust from statistical analyses (e.g., Plesch et al., 2014, from a set of closely spaced boreholes in the Los Angeles basin, CA, estimating H/V~25; Nakata and Beroza, 2015, using random-field model representations of a 3-D *P*-wave velocity model at Long Beach, CA, finding H/V~5). While these H/V measurements are based on analysis of representations of the crustal structure we here constrain the anisotropy from modeling regional wave propagation from the NKNTS to stations INCN and TJN. Figures 7 (INCN) and A6 (TJN) show waveform comparisons for the gradient model of small-scale heterogeneities with σ = 10% from the surface to a depth of 10 km, σ = 2% below a depth of 12.5 km, with H/V =1, 5, 7, 10 (Models 6, 10-12, Table 1). The model with no anisotropy (H/V=1) generates a Rayleigh wave deficient in higher frequencies and with larger amplitude than observed in the data. The Rayleigh wave for H/V values of 7 and 10, while limited to a narrower time window, also overpredicts the amplitude of the phase in the data. The (high-frequency) energy associated with the P_n

phases for the simulations with H/V = 1, 7, and 10 are larger than that for the data, in particular for H/V=7. The value of H/V that generates the synthetics in best agreement with data for both initial P waves and surface waves, is 5, in agreement with the results by Nakata and Beroza (2015).

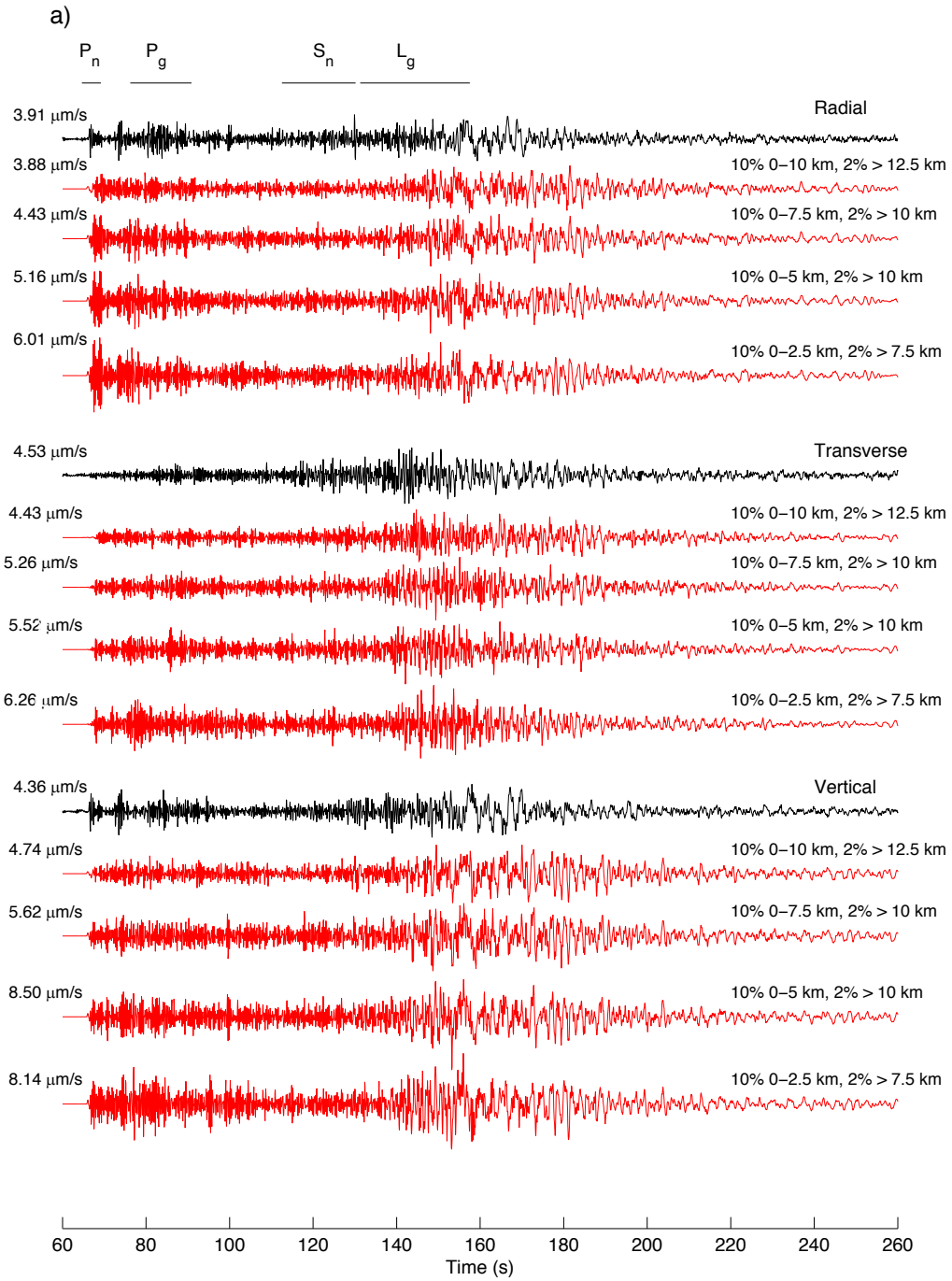

Figure 5. (top) Comparison of observed (black) and synthetic (red) waveforms at INCN for Models 6-9 (Table 1). ***The gradient models are all characterized by s = 10% from the surface to a depth of d1 km, s = 2% below a depth of d2 km, and a linear gradient in between. The values of d1 and d2 are listed by the synthetics. The bottom figure shows the comparison in the frequency domain for Model 6 (Table 1).***

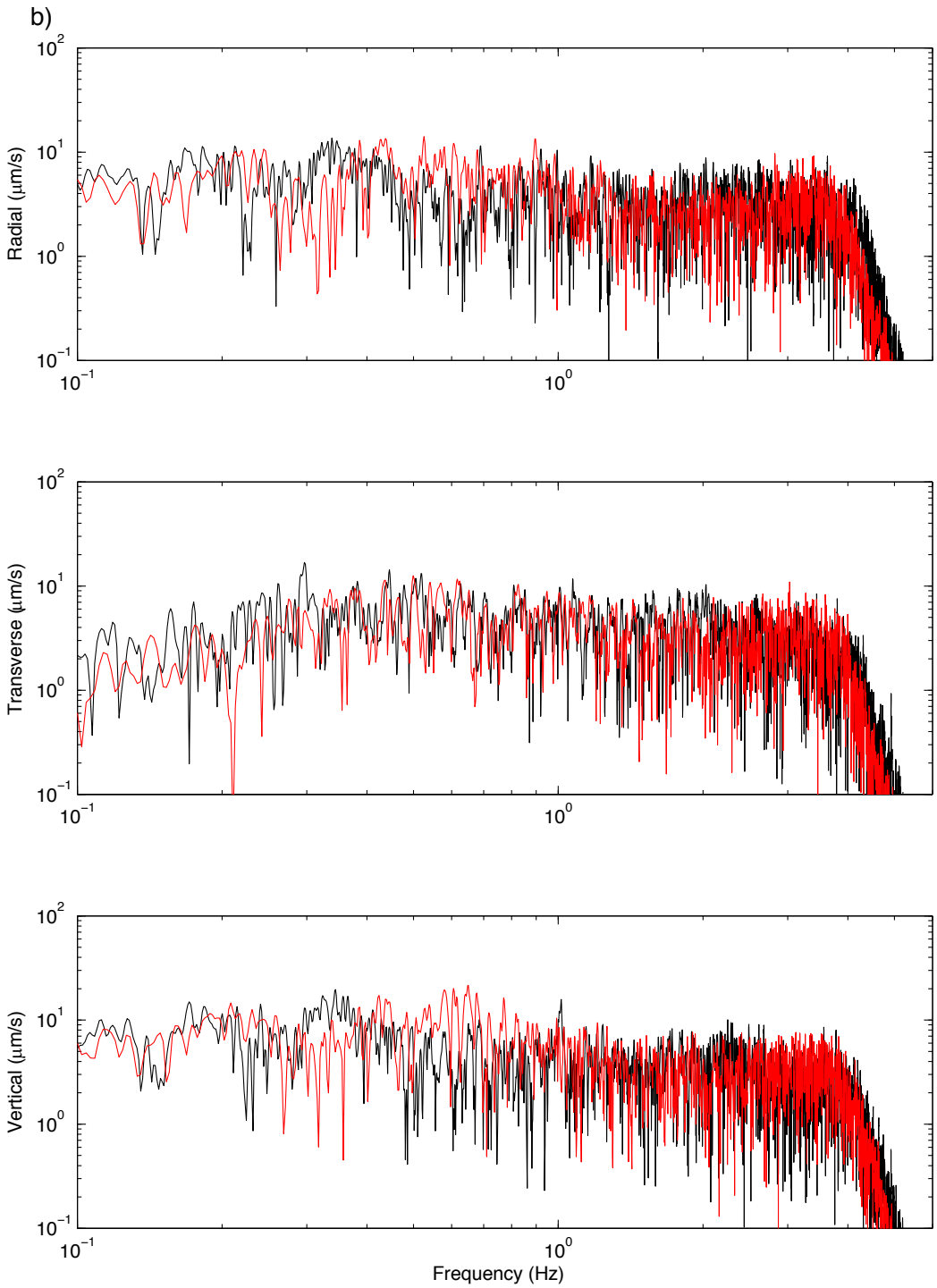

Figure 5 (continued). (top) Comparison of observed (black) and synthetic (red) waveforms at INCN for Models 6-9 (Table 1). ***The gradient models are all characterized by σ = 10% from the surface to a depth of d_1 km, σ = 2% below a depth of d_2 km, and a linear gradient in between. The values of d_1 and d_2 are listed by the synthetics. The bottom figure shows the comparison in the frequency domain for Model 6 (Table 1).***

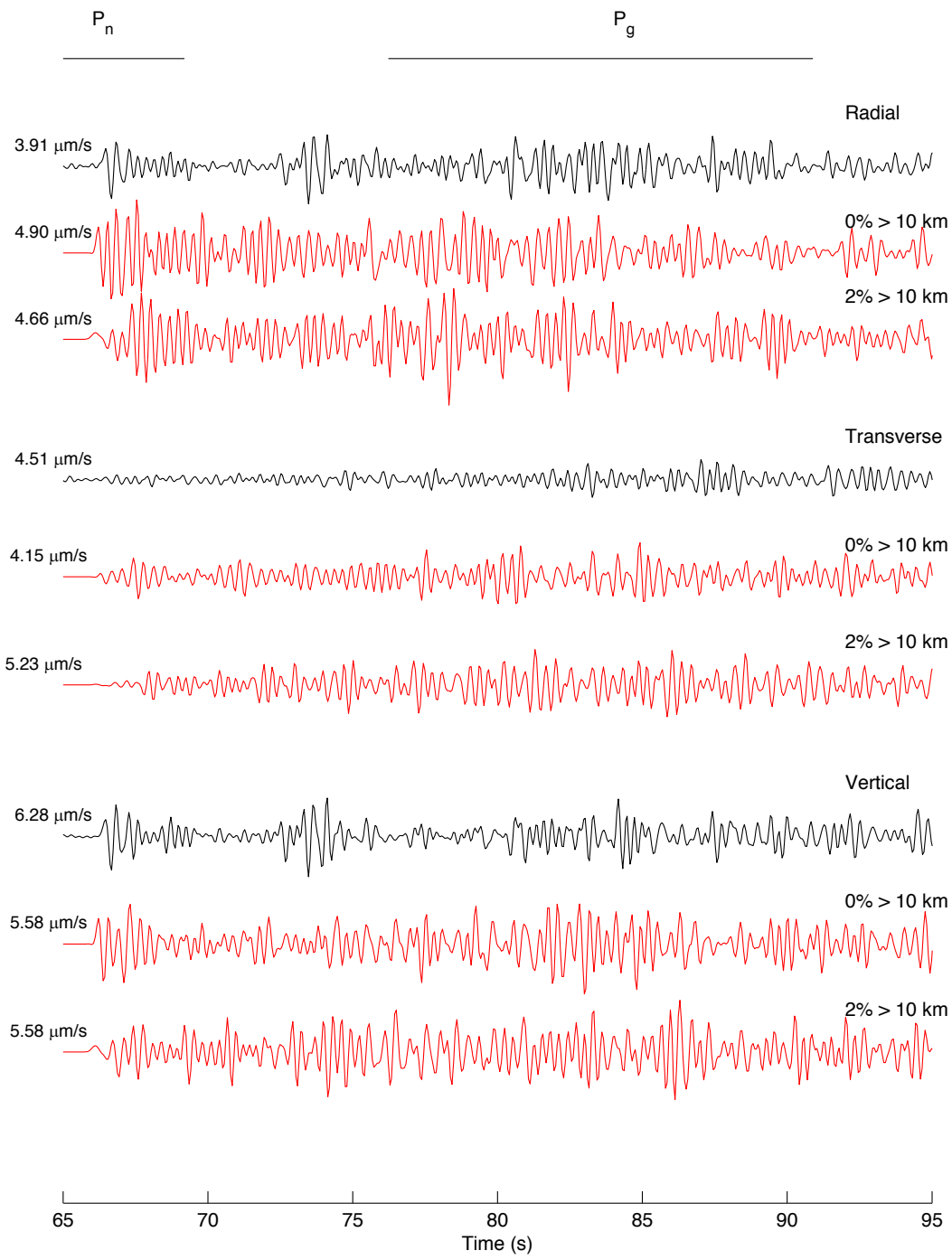

Figure 6. Zoom of the time domain comparison for INCN using Models 7 and 7a (Table 1). ***Peak velocities listed refer to the time interval shown.***

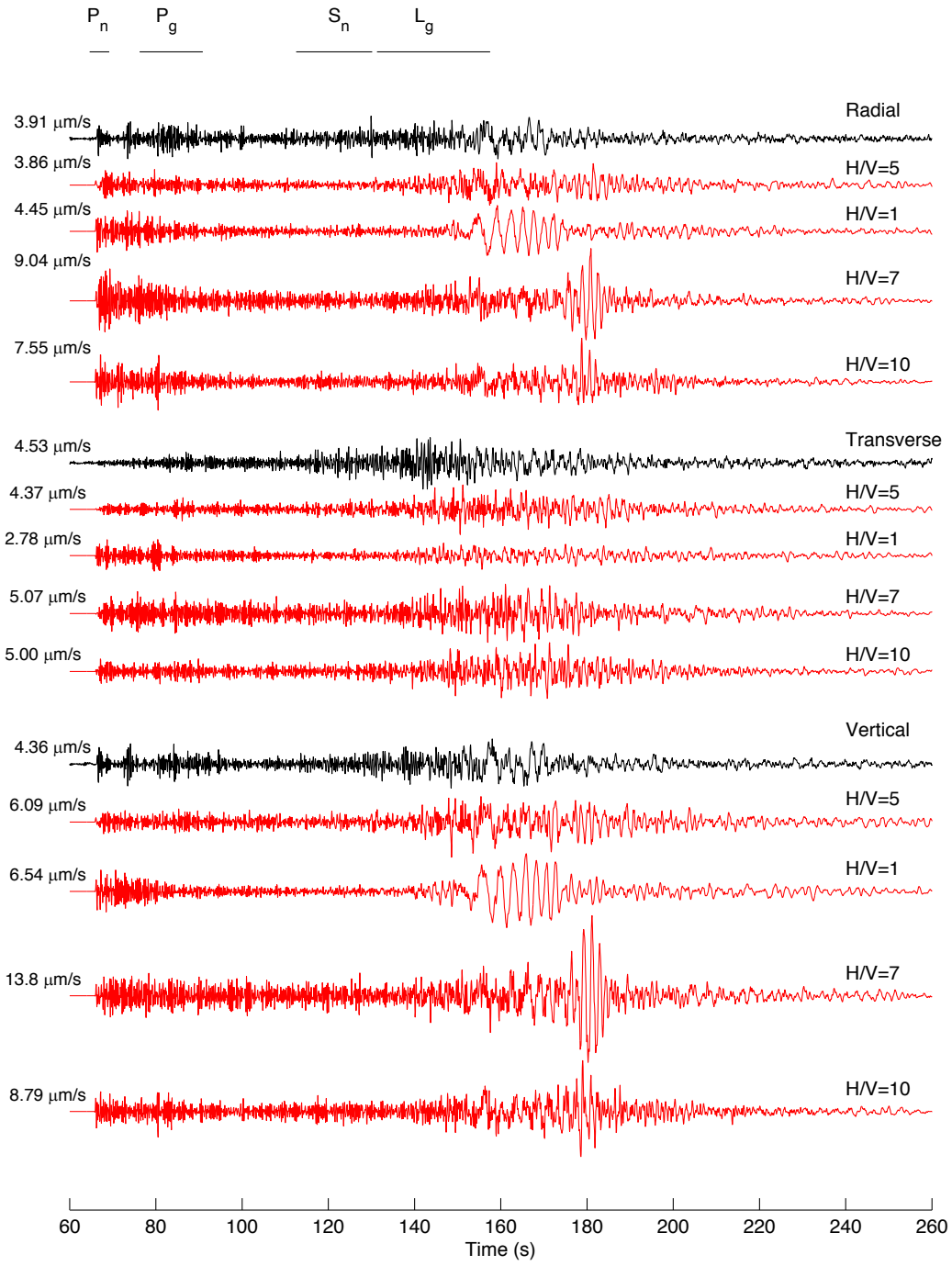

Figure 7. Comparison at INCN of the scattering effects from anisotropy in the small-scale heterogeneities, quantified by the ratio of horizontal-to-vertical dimensions of the velocity and density perturbations (H/V). ***Results for H/V=1, 5, 7, and 10 (Models 10, 6, 11 and 12, respectively, Table 1) are shown.***

3.6.5 Constraints on Correlation Length of the Small-scale Crustal and Mantle Heterogeneities.

Previous modeling studies that have included statistical models of small-scale heterogeneities have considered a tremendous range of correlation lengths for the velocity perturbations, from tens of meters to 10 km (see section **3.6.1**). Here, we test whether an optimal value for the correlation length of the crust and mantle between the NKNTS and INCN and TJN can be found, in terms of the match between data and synthetics at the two stations. Figures 8 and A7 show the waveform fits at INCN and TJN, respectively, for Q(f), ν, and σ of Model 6, and correlation length of 150 m, 1,000 m, 2,000 m, and 3,000 m (Models 13, 6, 14 and 15, Table 1). The synthetics for a = 150 m, 2,000 m and 3,000 m tend to generate large-amplitude Rayleigh waves (~160-180 s at INCN, ~200-230 s at TJN), with similarity to those obtained in Model 1 without small-scale heterogeneities (Figure 3). On the other hand, the synthetics obtained from the model with a = 1,000 m (Model 6) generally resembles the waveform characteristics of the data, with much smaller Rayleigh-wave amplitudes, as compared to those from the models with shorter and longer values of a. Based on this result, we adopt a value of 1,000 m as an average correlation length for the path between the NKNTS and the western North Korean Peninsula.

3.6.6 Near-source Scattering and Generation of S-wave Energy.

An explosive source with limited tectonic release and other near-source effects primarily generates compressional seismic energy (e.g., Ford et al., 2009; Shin et al., 2010). However, records from explosive sources at regional distances often contain considerable S-wave energy (as is the case for the observed transverse component at INCN and TJN in our models). Our simulations have shown that crustal and mantle scattering processes from small-scale heterogeneities can explain almost all of the S-wave and Love wave energy, e.g., the main phases on the transverse component. The FD modeling technique allows us to investigate which fraction of the S-wave energy is generated in the near-source region.

Toward this goal, Figures 9 (INCN) and A8 (TJN) compare synthetics with small-scale heterogeneities added with the gradient from Model 6 (Table 1), where the small-scale heterogeneities are omitted within a spherical volume with radii of 0, 1, 5 and 10 km. At a first glance, the synthetics for the four different models are very similar, in both amplitude and general characteristics of the phases. The synthetics for the model with R=0 km are visually almost identical to those with R = 1 and 5 km, while smaller variations in phase and a slight decrease in peak amplitude start to appear in the synthetics for R = 10. These results apply to all three components, including the transverse component, with predominantly S-wave energy and where the contribution from an isotropic source is expected to be minimal. Thus, Figures 9 and A8 suggest that scattering within a narrow region around the source contributes negligibly to the S-wave energy recorded at INCN and TJN.

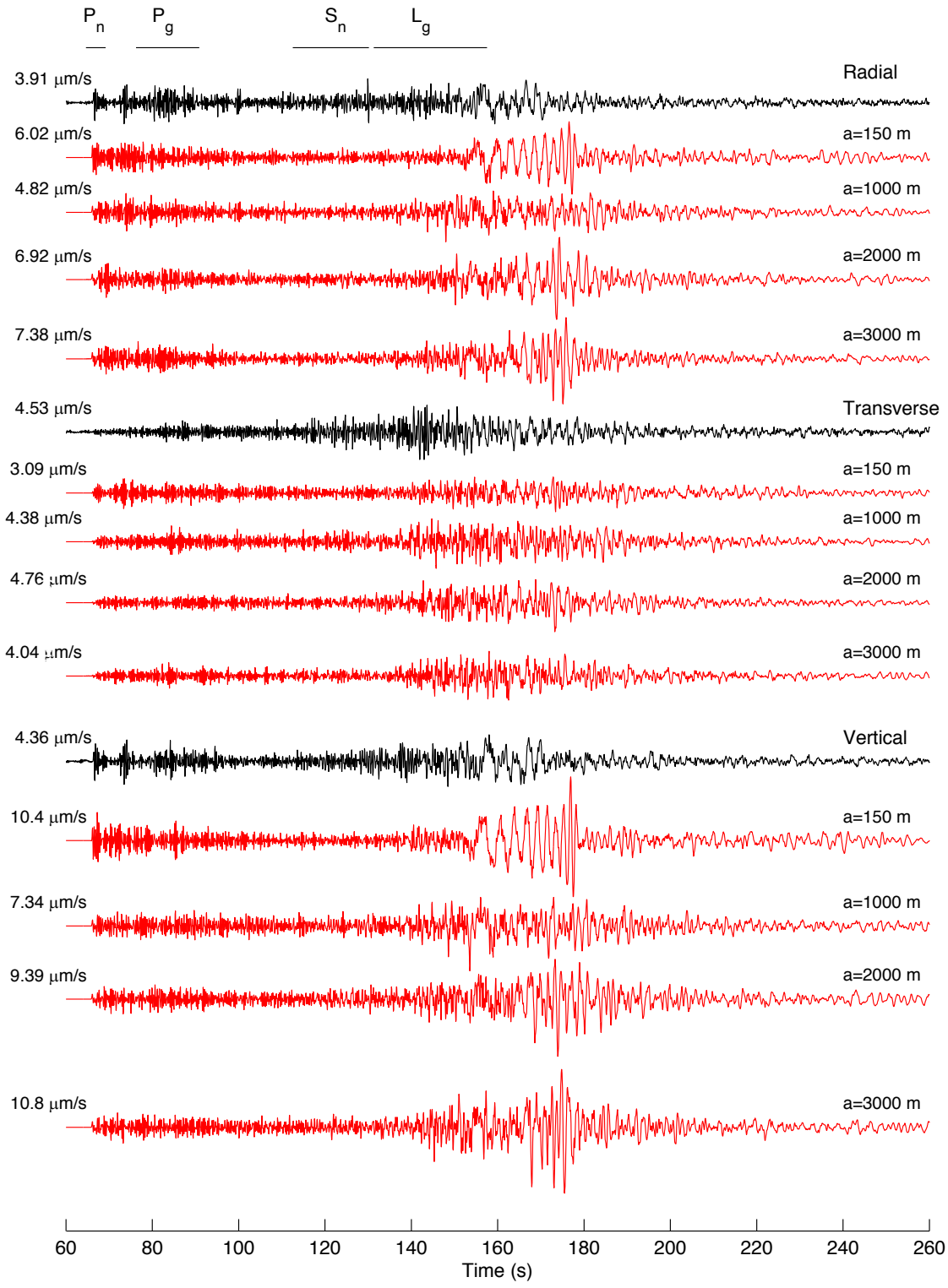

Figure 8. Comparison at INCN of the scattering effects from different correlation length in the distribution of small scale heterogeneities (150 m, 1,000 m, 2,000 m, and 3,000 m) as defined by Models 13, 6a, 14 and 15 (Table 1).

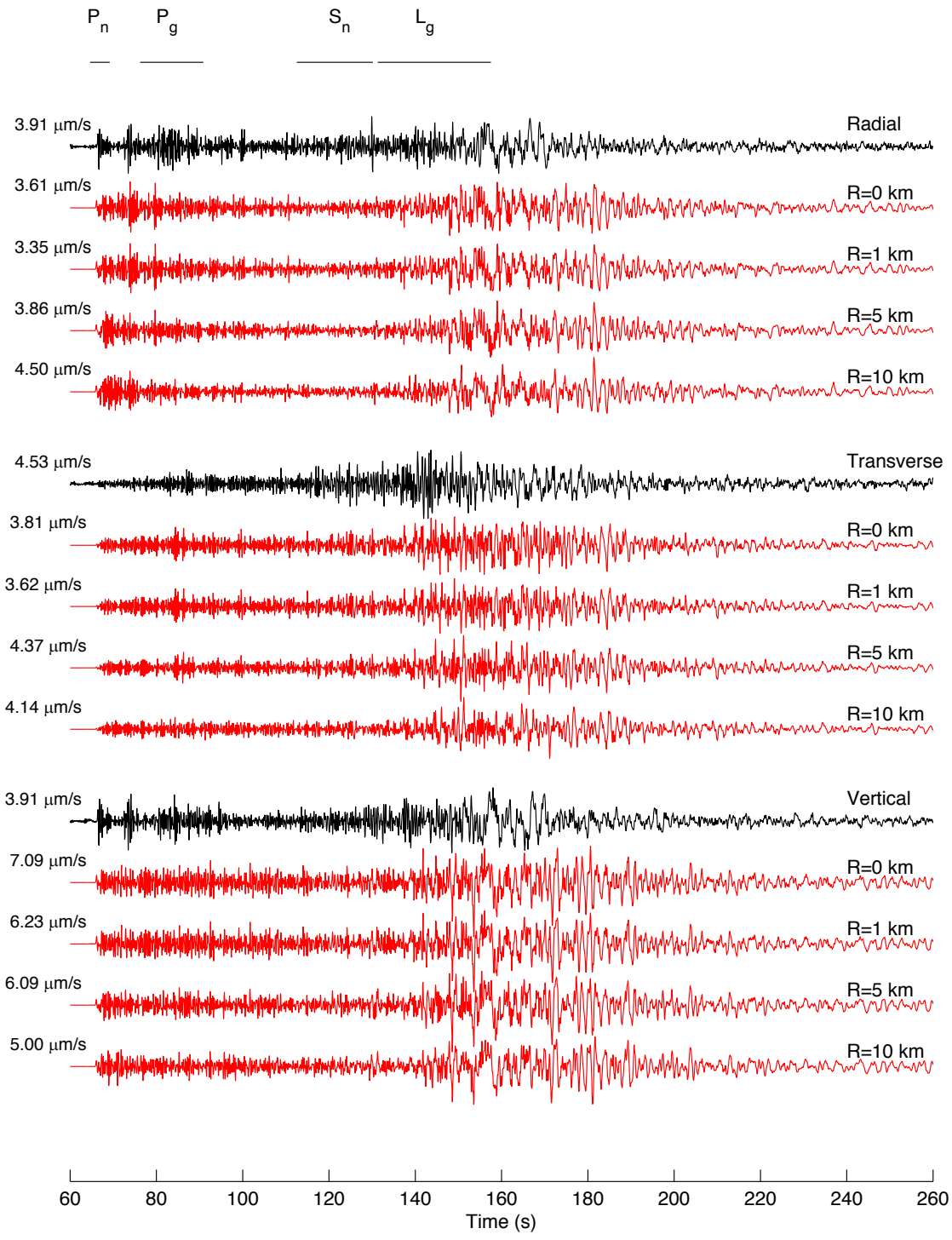

Figure 9. Significance of near-source scattering effects from small-scale heterogeneities at INCN. ***The small-scale heterogeneities (6, Table 1) have been removed within radii (R) of 0-10 km from source, listed by the synthetics.***

Figure 10 shows snapshots of velocity wave propagation in Model 6 (Table 1). The contrast of the wavefield in Figure 10 compared to that in Figure 3 is striking, primarily due to the amount of crustal scattering generated by the small-scale heterogeneities. At 27.5s, P-to-S and P-to-P scattering dominates the area between the P waves and surface waves. The surface waves, characterized by large-amplitude coherent wave trains in the model without small-scale heterogeneities (Figure 3), appear as a 100 km+ wide band of scattered energy at 82.5s. Here, the amplitudes diminish away from a central high, indicating the presence of both forward and backward scattering. At later times (82.5 s and 137.5 s), the largest scattered surface waves occur offshore east for the Korean Peninsula in the lower velocity material.

3.7 Data and Resources

We use a GPU-enabled fourth-order accurate staggered-grid FD method (AWP-ODC-GPU, Cui et al., 2013, open source referenced (BSD-2) for our NKNTS wave propagation simulations. 350 s of wave propagation in the 24 billion grid model using 2500 GPUs required 80-100 minutes of Wall-clock time on the ORNL Titan supercomputer.

4. RESULTS AND DISCUSSION

The stochastic nature of the velocity and density perturbations in the underlying crustal and mantle structure allows us to model the statistics of the resulting synthetics, while the details of the individual phases and coda depends on the realization of the specific distribution of small-scale heterogeneities. For this reason, an infinite set of ground motion synthetics can be derived from a given set of von Karman parameters. To estimate the range of ground motions to be expected from the possible realizations associated with the statistical distributions generated in this study, Figures 11 (INCN) and A9 (TJN) compare synthetics for 5 realizations the same gradient model of small-scale heterogeneities (Models 16-20, Table 1). As expected, the general characteristics including arrival times and amplitude of the simulated waveforms discussed in this article persist among the realizations. For example, the variation of the peak amplitude among the 5 realizations is less than 65%. It is interesting to note, however, that the amplitude of the individual phases can vary by a much larger amount. This result suggests that it is necessary to use an ensemble of simulations generated from different realizations of von Karman distributions of small-scale heterogeneities, in particular for applications depending specifically on P and S amplitudes, such as source discrimination.

Baker et al. (2012) reviewed the various mechanisms published for generating S wave energy from shallow explosions in relatively high-velocity crust (such as the crust between the NKNTS and INCN and TJN). This review concluded that the majority of the S energy is generated by the non-spherical component of the source volume, as opposed to regional scattering. Their results appear to contradict those from this study, where our simulations show that an insignificant amount of the S-wave energy arriving at INCN and TJN is generated by scattering within 10 km of the source. Pitarka et al. (2015) used 0-10 Hz numerical simulations and data from the Source Physics Experiment (SPE) at the Nevada National Security site to analyze the generation of S wave energy at very-near

source distances (<1 km). They found that a large part of the S wave energy present in the simulations were generated near the source. Further analysis is needed to explain the reasons for the different conclusions related to near-source S wave generation obtained here.

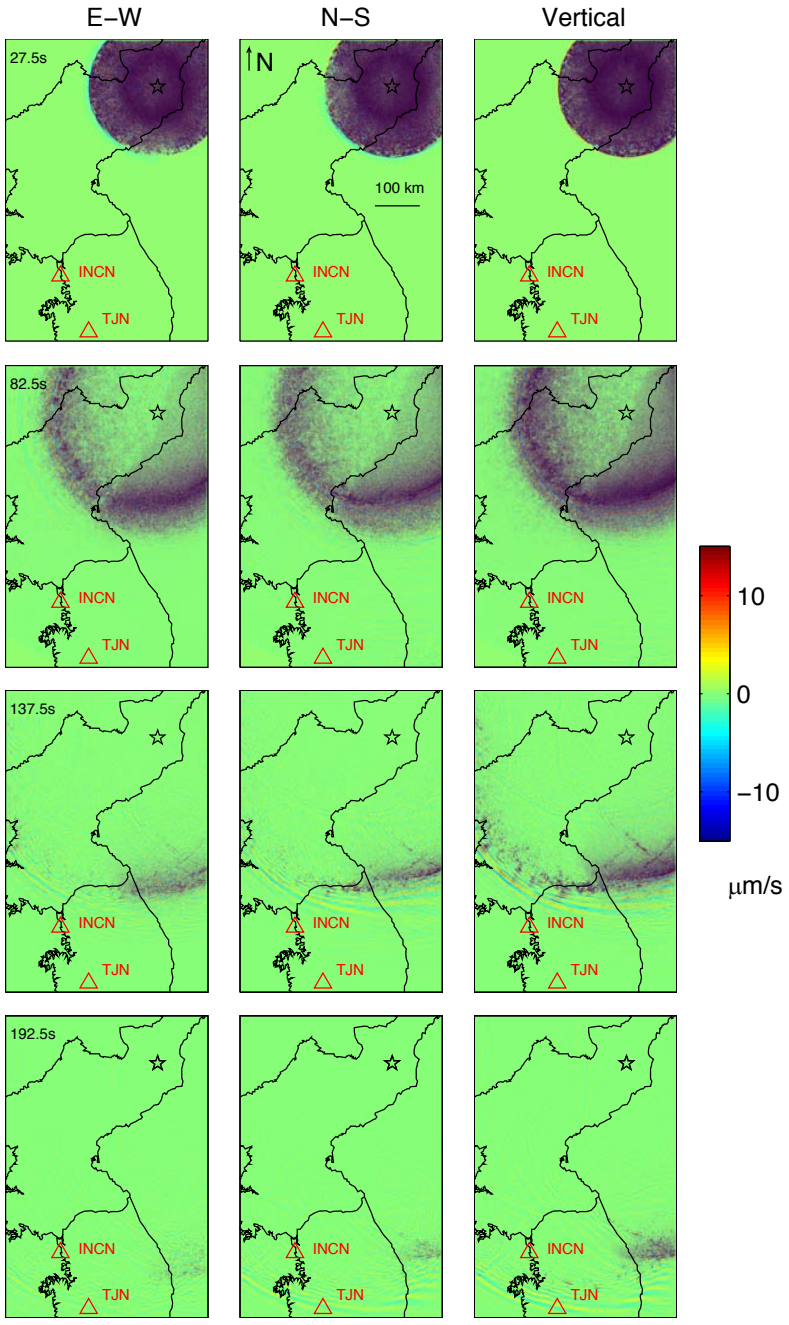

Figure 10. Snapshots of wave propagation for Model 6 (Table 1).

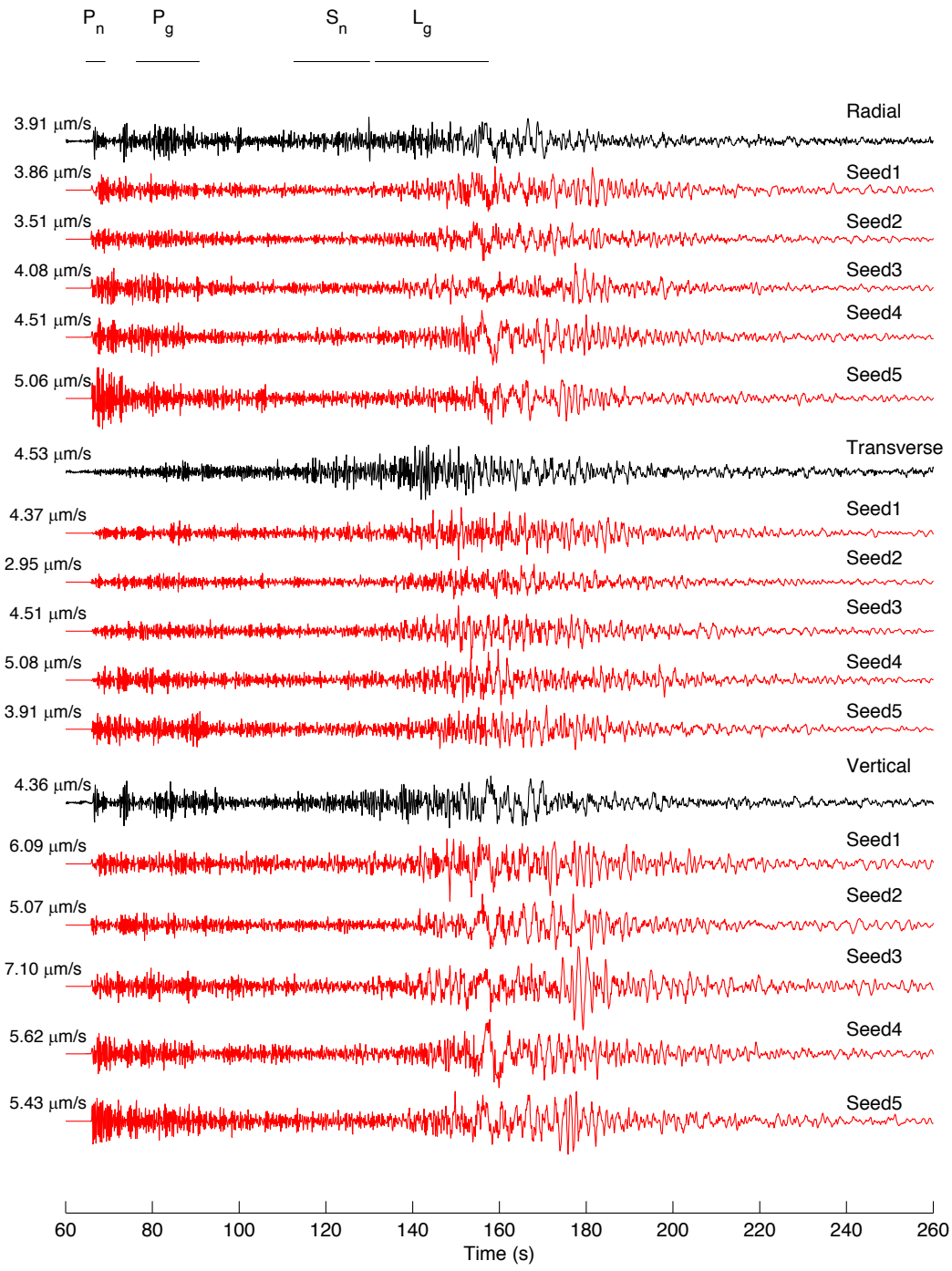

Figure 11. Comparison of data to synthetics generated from a 5-realization ensemble of statistical models of small-scale heterogeneities with different seed numbers at INCN. ***All simulations use the Q(f), H, a, H/V and σ of Models 16-20 (Table 1).***

Topographic scattering was omitted in the simulations carried out in our study, and thus was not necessary to obtain the waveform fits presented here. However, Rodgers et al. (2010) found that topographic scattering can have significant effects on the resulting wavefield, including enhancement of energy propagation near the source, surface wave amplification, and SV and SH-wave polarization simulated for 0-8 Hz wave propagation from the 2006 and 2009 North Korean nuclear tests. Their simulations using different proposed locations of the sources a few kilometers apart generated significantly different wavefields due to the variation-specific source-coupling with local topography. Unfortunately, no observations were available within their 40 km x 40 km region for comparison. The largest topographic scattering effects were generated for frequencies larger than the 4 Hz used in our study. On the other hand, Takemura et al. (2015) used 3D 0-4 Hz FD simulations including both surface topography and small-scale heterogeneities to distances of 80 km from explosive and earthquake sources. They found, in general agreement with our results, that the primary source of scattered energy was small-scale heterogeneities in the crust, while the cumulative effect of surface topography is limited over long distances. Future studies should further delineate the relative contributions of small-scale heterogeneities and surface topography on seismic waveforms for regional propagation distances.

We found that a vertical correlation length of 1,000 m represented an optimal value based on trial-and-error tests within a range of 150-3,000 m. Our preferred value of a=1,000 m is longer than that estimated from sonic logs by Savran and Olsen (2016) and Plesch et al. (2014) (<150 m). However, the efficacy of the longer correlation length in reproducing the INCN and TJN waveforms is not too surprising, as the detailed sonic logs with sample spacings < 1 m may be biased toward smaller (high frequency) correlation lengths, and the rather smooth SALSA3D is deficient in most length scales less than ~10 kilometer or more.

In order to reach a maximum frequency of 4 Hz for the simulations in this study (with a minimum of 6.25 points per minimum S-wave length), we have limited the minimum V_s in the crustal models to 2,500 m/s. This artificial constraint is implemented at a grid point by resetting V_s to 2,500 m/s, and replacing V_p by 2,500 m/s times the V_p/V_s ratio at the grid point. This modification has little effect within the N-S oriented band within the Korean peninsula where V_s^{min} is already near 3,100 m/s (see Fig. A10), in the general path between the NKNTS and western South Korea. However, the upper ~3.1 km of the continental shelf to the east of this band has V_s as low as 969 m/s, and may need to be included when modeling data further east.

The accuracy of the attenuation and scattering parameters on the Korean Peninsula estimated in this study relies on an estimate of the magnitude of the 2009 NKNTS explosion. We have estimated the moment of our isotropic source function by comparing the low-frequency spectral amplitude for synthetics and data at INCN and TJN ($1.58e^{15}$ Nm, M_w=4.1). This estimate of the source magnitude is in agreement with Ford (2009), supporting our results. A slightly refined estimate of the source magnitude obtained using additional data constraints is not expected to significantly change the conclusions of this study.

Our results demonstrate that state-of-the-art high-frequency 3D wave propagation simulations using high-performance computing can reproduce the general character of records for stations located hundreds of kilometers from the source. We recommend that

future work continue to take advantage of these computing capabilities to refine the estimates of the parameters for Q(f) and small-scale heterogeneities with systematic inversion methods, rather than trial and error modeling, to further minimize any bias from inter-dependency between modeling parameters. The results of the simulations, where synthetics are available on a regular grid at the surface, provide a magnificent 'dataset' to test methods for discriminating explosive and earthquake sources as a function of distance from the source and azimuth. Such analysis is currently ongoing.

5. CONCLUSIONS

Recent advances in high-performance computing has facilitated fully deterministic 3D elasto-dynamic simulations of regional wave propagation (400 km+). We demonstrate these capabilities by modeling time histories for the 2009 North Korea nuclear explosion at stations INCN and TJN in South Korea for frequencies up to 4 Hz in the Sandia/Los Alamos National Laboratory SALSA3D velocity model. Comparison of the synthetics and data show that the SALSA3D model fails to reproduce the main characteristics of the data for this bandwidth. In particular, the synthetics grossly overpredict Rayleigh wave amplitudes and underpredict the amplitudes of the coda. On the other hand, the addition to SALSA3D of small-scale perturbations of the P and S velocities and densities following a von Karman distribution with correlation lengths of ~1,000 m, Hurst number of 0.1, and horizontal-to-vertical anisotropy of ~5 improves the fit considerably. The results show that the wave propagation along the 400 km+ path from the 2009 NKNTS to INCN and TJN is strongly sensitive to the parameters of the small-scale crustal and mantle heterogeneities, as well as the frequency-dependent attenuation.

Our simulations show a strong depth dependency of the strength of the small-scale heterogeneities on the signature of the synthetics simulated at INCN and TJN from the NKNTS with constraints from data. In particular, models with a gradient in the strength of the velocity and density perturbations, and strong scattering (10%) limited to the top 7.5-10 km of the crust, tend to provide the synthetics with the best fit to data. Scattering contributions from deeper depths is shown to generate P_n and P_g amplitudes much below those for the data at the two stations. Specifically, the amplitude at the onset of the P_n phase can be significantly affected even for a standard deviation as low as 2% of the small-scale velocity and density perturbations with respect to the background SALSA3D variation in the lower crust and upper mantle. This result is important for methods used to discriminate between explosive and earthquake sources based on the amplitudes of P and S waves. In addition, the best fits are obtained for a horizontal-to-vertical anisotropy of the small-scale heterogeneities of about 5.

We used trial-and-error modeling with constant Q below a threshold frequency (1 Hz) and frequency-dependent Q following a power law for higher frequencies to constrain the anelastic attenuation parameters on the Korean Peninsula. The results show that constant Q of 200-350 below 1 Hz and a power-law exponent of ~0.3 for both P and S-waves generate synthetics in best agreement with the data.

The results of simulations where the small-scale heterogeneities are omitted in the close vicinity of the source indicate that a very small amount of scattering from the near-source area accumulates over the regional path. Our study suggests that the majority of the seismic energy recorded on the transverse component of the recorded waveforms is generated by P-S wave scattering primarily in the upper crust along the 400 km+ path from the source to the stations.

REFERENCES

Baker, G.E., J.L. Stevens, and H. Xu. (2012), Explosion shear-wave generation in high-velocity source media, *Bull. Seis. Soc. Am.*, **102**, 4, pp. 1301-1319, doi: 10.1785/0120110119.

Begnaud, M. L., S. Ballard, C. J. Young, J. R. Hipp, A. V. Encarnacao, W. S. Phillips, E. P. Chael, and C. A. Rowe (2012), Validating a global 3D P-velocity model of the Earth's crust and mantle for improved event location, in Proc. of the 2012 Monitoring Research Review: Ground-Based Nuclear Explosion Monitoring Technologies, Albuquerque, NM, pp. 200-209.

Bielak, J., R.W. Graves, K.B. Olsen, R. Taborda, L. Ramirez-Guzman, S.M. Day, G.P. Ely, D. Roten, T.H. Jordan, P.J. Maechling, J. Urbanic, Y. Cui, and G. Juve (2010), The ShakeOut earthquake scenario: Verification of three simulation sets, *Geophysical Journal International,* **180**, pp. 375-404, doi: 10.1111/ j.1365-246X.2009.04417.x.

Birch, F. (1961), The velocity of compressional waves in rocks to 10 kilobars, Part 2, *Journal of Geophysical Research,* **66** (7), pp. 2199-2224.

Cui, Y., E. Poyraz, K.B. Olsen, J. Zhou, K. Withers, S. Callaghan, J. Larkin, C. Guest, D. Choi, A. Chourasia, Z. Shi, S.M. Day, J.P. Maechling, and T.H. Jordan (2013), Physics-based seismic hazard analysis on petascale heterogeneous supercomputers, Procs, Supercomputing Conference, Denver, CO, 2013.

Cui, Y., K. Olsen, T. Jordan, K. Lee, J. Zhou, P. Small, D. Roten, G. Ely, D. Panda, A. Chourasia, et al. (2010), Scalable earthquake simulation on petascale supercomputers, Procs. Supercomputing Conference, New Orleans, LA, 13-19 November.

Day, S. M., R. W. Graves, J. Bielak, D. Dreger, S. Larsen, K. B. Olsen, A. Pitarka, and L. Ramirez-Guzman (2008), Model for basin effects on long-period response spectra in southern California, *Earthquake Spectra,* **24**, pp. 257-277.

De, G.S., D.F. Winterstein, and M.A. Meadows (1994), Comparison of *P* and *S*-wave velocities and *Q*'s from VSP and sonic log data, *Geophysics,* **59**(10), pp. 1512-1529.

Dolan, S., C. Bean, and B. Riollet (1998), The broad-band fractal nature of heterogeneity in the upper crust from petrophysical logs, *Geophys. J. Int.,* **132**(3), pp. 489-507.

Ford, S.R., D.S. Dreger, and W.R. Walter (2009), Source analysis of the Memorial Day explosion, Kimchaek, North Korea, *Geophysical Research Letters,* **36,** L21304, doi:10.1029/2009GL040003.

Ford, S.R., W.S. Phillips, W.R. Walter, M.E. Pasyanos, K. Mayeda, and D.S. Dreger (2010), Attenuation Tomography of the Yellow Sea/Korean Peninsula from Coda-source normalized and direct Lg Amplitudes, *Pure Appl. Geophys*., **167**, pp. 1163-1170, DOI 10.1007/s00024-009-0023-2.

Frankel, A. and R.W. Clayton (1986), Finite difference simulations of seismic scattering: implications for the propagation of short-period seismic waves in the crust and models of crustal heterogeneity, *J. Geophys. Res.,* **91**(B6), pp. 6465-6489.

Hartzell, S., S. Harmsen, and A. Frankel (2010), Effects of 3D random correlated velocity perturbations on predicted ground motions, *Bull. seism. Soc. Am.,* **100**(4), pp. 1415-1426.

Holliger, K. and A.R. Levander (1992), A stochastic view of lower crustal fabric based on evidence from the Ivrea Zone, *Geophys. Res. Lett.*, **19**(11), pp.1153-1156.
Holliger, K. (1996), Upper-crustal seismic velocity heterogeneity as derived from a variety of P-wave sonic logs, *Geophys. J. Int.*, **125**(3), pp. 813-829.
Holliger, K. (1997), Seismic scattering in the upper crystalline crust based on evidence from sonic logs, *Geophys. J. Int.*, **128**(1), pp. 65–72.
Hong, T-K. and J. Rhie (2009), Regional source scaling of the 9 October 2006 underground nuclear explosion in North Korea, *Bull. Seis. Soc. Am.* **99**, 4, 2523- 2540.
Imperatori, W. and P.M. Mai (2013), Broad-band near-field ground motion simulations in 3-dimensional scattering media, *Geophys. J. Int.*, **192**(2), pp. 725-744.
Jacobsen, B.H. and K.B. Olsen (2011), Spatial variability of ground motion amplification from low-velocity sediments including fractal inhomogeneities with special reference to the Southern California basins, EGU General Assembly 2011, Vienna, Austria.
Lekic, V., J. Matas, M. Panning, and B. Romanowicz (2009), Measurement and implications of frequency dependence of attenuation, *Earth Planet. Sci. Lett.*, **282**, pp. 285-293.
Levander, A.R., England, R.W., Smith, S.K., Hobbs, R.W., Goff, J.A. & Holliger, K. (1994), Stochastic characterization and seismic response of upper and middle crustal rocks based on the Lewisian Gneiss Complex, Scotland, *Geophys. J. Int.*, **119**(1), pp. 243-259.
McNamara, D., M. Meremonte, J. Z. Maharrey, S.-L. Mildore, J. R. Altidore, D. Anglade, S. E. Hough, D. Given, H. Benz, L. Gee, et al. (2012), Frequency-dependent seismic attenuation within the Hispaniola Island region of the Caribbean Sea, *Bull. Seismol. Soc. Am.*, **102**, pp. 773-782, ISSN: 0037–1106.
Mitchell, B.J., Y. Pan, J. Xie, and L. Cong (1997), Lg coda Q variation across Eurasia and ts relation to crustal evolution, *Jour. Geophys. Res.*, **102**, No B10, pp. 22,767-22,779.
Nafe, J. E., and C. L. Drake (1957), Physical properties of marine sediments, in *The Sea*, M. N. Hill, (Editor) Vol. 3, Interscience, New York, NY, pp.794-815.
Nakata, N. and G. Beroza (2015), Stochastic characterization of mesoscale seismic velocity heterogeneity in Long Beach, CA, *Geophys. Jour. Int.* **203**, pp. 2049-2054.
Olsen, K.B. (1994), Simulation of three-dimensional wave propagation in the Salt Lake Basin, Ph.D. Thesis, University of Utah, Salt Lake City, UT.
Olsen, K.B. (2000), Site Amplification in the Los Angeles Basin from 3D Modeling of Ground Motion, *Bull. Seis. Soc. Am.*, **90**, pp. S77-S94.
Olsen, K.B, and R. Takedatsu (2015), The SDSU Broadband Ground-Motion Generation Module BBtoolbox Version 1.5, *Seism. Res. Lett.*, **86**, 1, pp. 81-88.
Patton, H.J. and F.V. Pabian (2014), Comment on "Advanced seismic analysis of the source characteristics of the 2006 and 2009 North Korean nuclear tests," by J.R. Murphy, J.L. Stevens, B.C. Kohl, and T.J. Bennett, *Bull. Seis. Soc. Am.*, **104**, 4, pp. 2104-2110.

Phillips, W. S., K. M. Mayeda, and L. Malagnini (2013), How to invert multi-band, regional phase amplitudes for 2-D attenuation and source parameters: Tests using the USArray, *Pure Appl. Geophys.*, **171**, pp. 469-484.

Pitarka, A., R. J. Mellors, W. R. Walter, S. Ezzedine, O. Vorobiev, T. Antoun, J. L. Wagoner, E. M. Matzel, S. R. Ford, A. J. Rodgers, L. Glenn, and M. Pasyanos (2015), Analysis of Ground Motion from An Underground Chemical Explosion, *Bull. Seis. Soc. Am.*, **105**, 5, pp. 2390-2410, doi: 10.1785/0120150066.

Plesch, A., J.H. Shaw, X. Song, and T.H. Jordan (2014), Stochastic descriptions of fine-scale basin velocity structure from well logs and the SCEC Community Velocity Model (CVMH), *Seism. Res. Lett.*, **85** (2), p. 382.

Raoof, M., R. Herrmann, and L. Malagnini (1999), Attenuation and excitation of three-component ground motion in southern California, *Bull. Seismol. Soc. Am.*, **89**, pp. 888-902.

Rodgers, A., N. A. Petersson, and B. Sjogreen (2010), Simulation of topographic effects on seismic waves from shallow explosions near the North Korean nuclear test site with emphasis on shear wave generation, *J. Geophys. Res.*, **115**, no. B11, doi: 10.1029/2010JB007707.

Savran, W.H. and K.B. Olsen (2016), Model for Small-Scale Crustal Heterogeneity in Los Angeles Basin Based on Inversion of Sonic Log Data, *Geophys. Res. Lett.*, **205**, pp. 856-863.

Shin, J. S., D.-H. Sheen, and G. Kim (2010), Regional observations of the second North Korean test on 2009 May 25, *Geophys. J. Int,*. **180**, pp. 243-250.

Takemura, S., T. Furumura and T. Maeda (2015), Scattering of high-frequency seismic waves caused by irregular surface topography and small-scale velocity inhomogeneity, *Geophys. Jour. Int.*, **201**, pp. 459-474.

Tatarski, V.I. (1961), Wave propagation in a turbulent medium, McGraw-Hill, New York, NY.

Withers, K.B., K.B. Olsen and S.M. Day (2015), Memory Efficient Simulation of Frequency Dependent Q, *Bull, Seis. Soc. Am,*. **105**, pp. 3129-3142, doi: 10.1785/0120150020.

Wu, R.S., Z. Xu, and X.-P Li (1994), Heterogeneity spectrum and scale-anisotropy in the upper crust revealed by the German Continental Deep-Drilling (KTB) Holes, *Geophys. Res. Lett.*, **21**(10), pp. 911-914.

Xie, J., Z. Wu, R. Liu, D. Schaff, Y. Liu, and J. Liang (2006), Tomographic regionalization of crustal Lg Q in eastern Eurasia, *Geophys. Res. Lett.*, **33**, L03315, pp. 1-4.

APPENDIX A

List of Figures

This Appendix contains description of the source time function used in the simulations, and comparison of data to synthetics at station TJN for the same tests as reported for INCN in the main text.

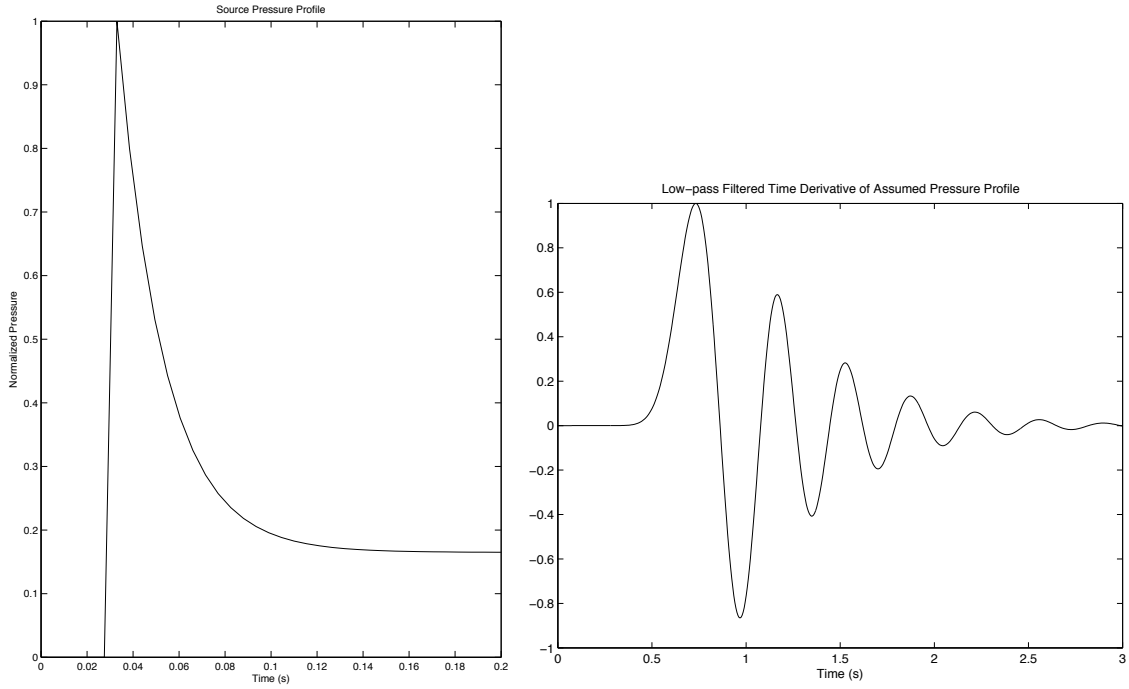

Figure A1. Assumed source (left) pressure profile (exp(-50*dt)+0.15, where dt is the time step in the simulation), and (right) its low-pass time derivative, inserted into the FD simulation.

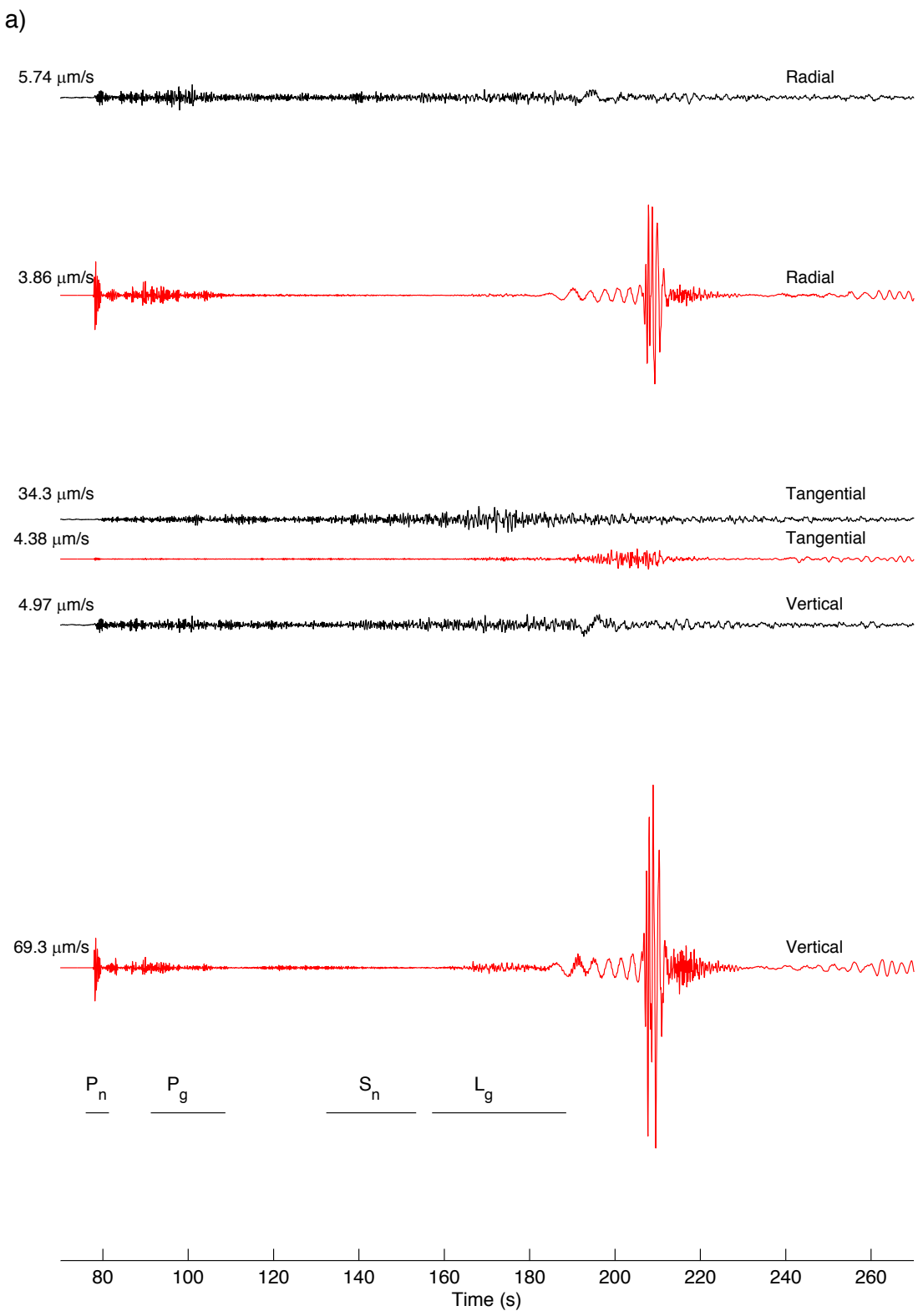

Figure A2. Comparison of observed (black) and synthetic waveforms at TJN for the SALSA3D model with Model 1 (Table 1) in (a) time and (b) frequency domains.

b)

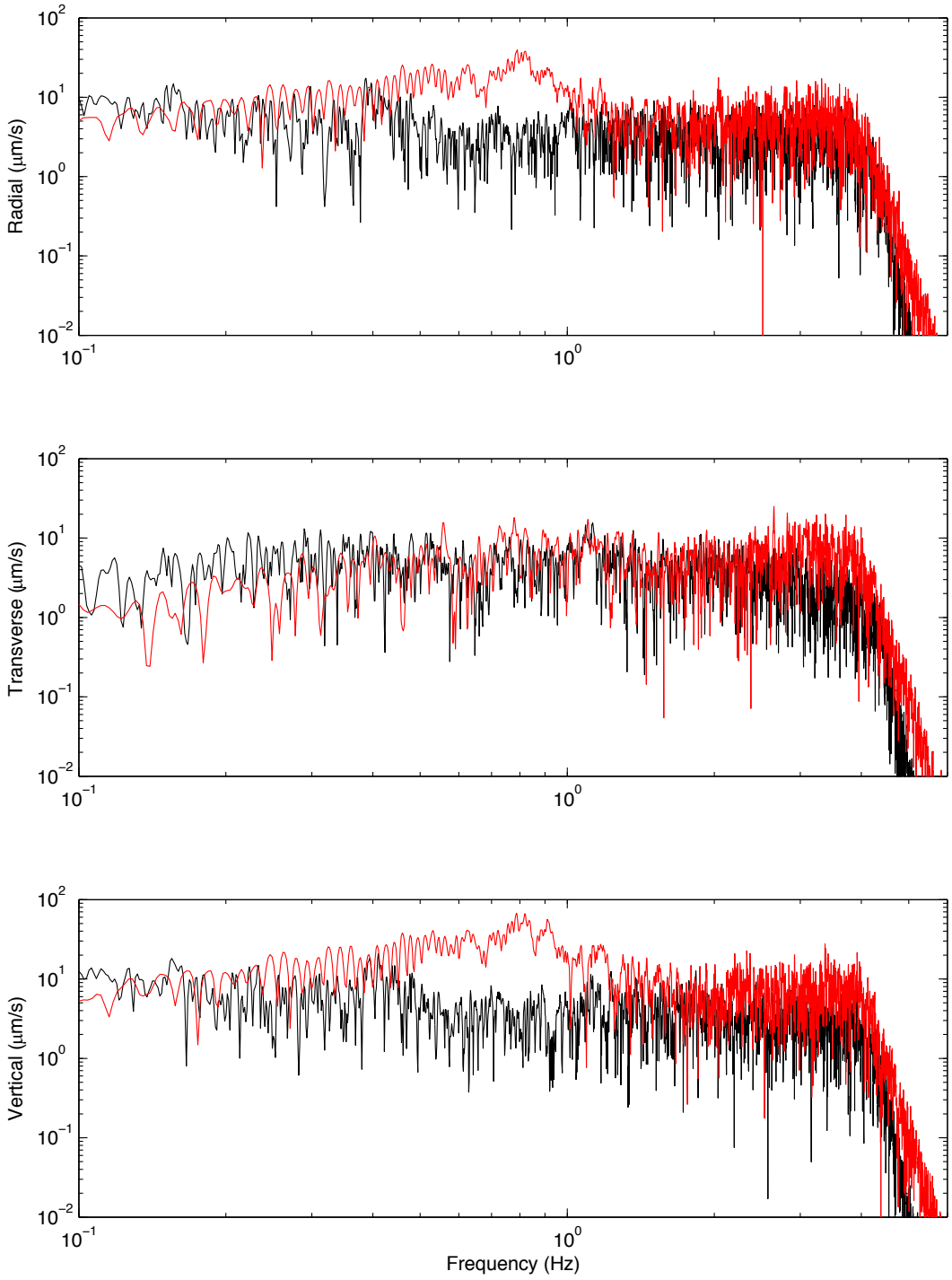

Figure A2 (continued). Comparison of observed (black) and synthetic waveforms at TJN for the SALSA3D model with Model 1 (Table 1) in (a) time and (b) frequency domains.

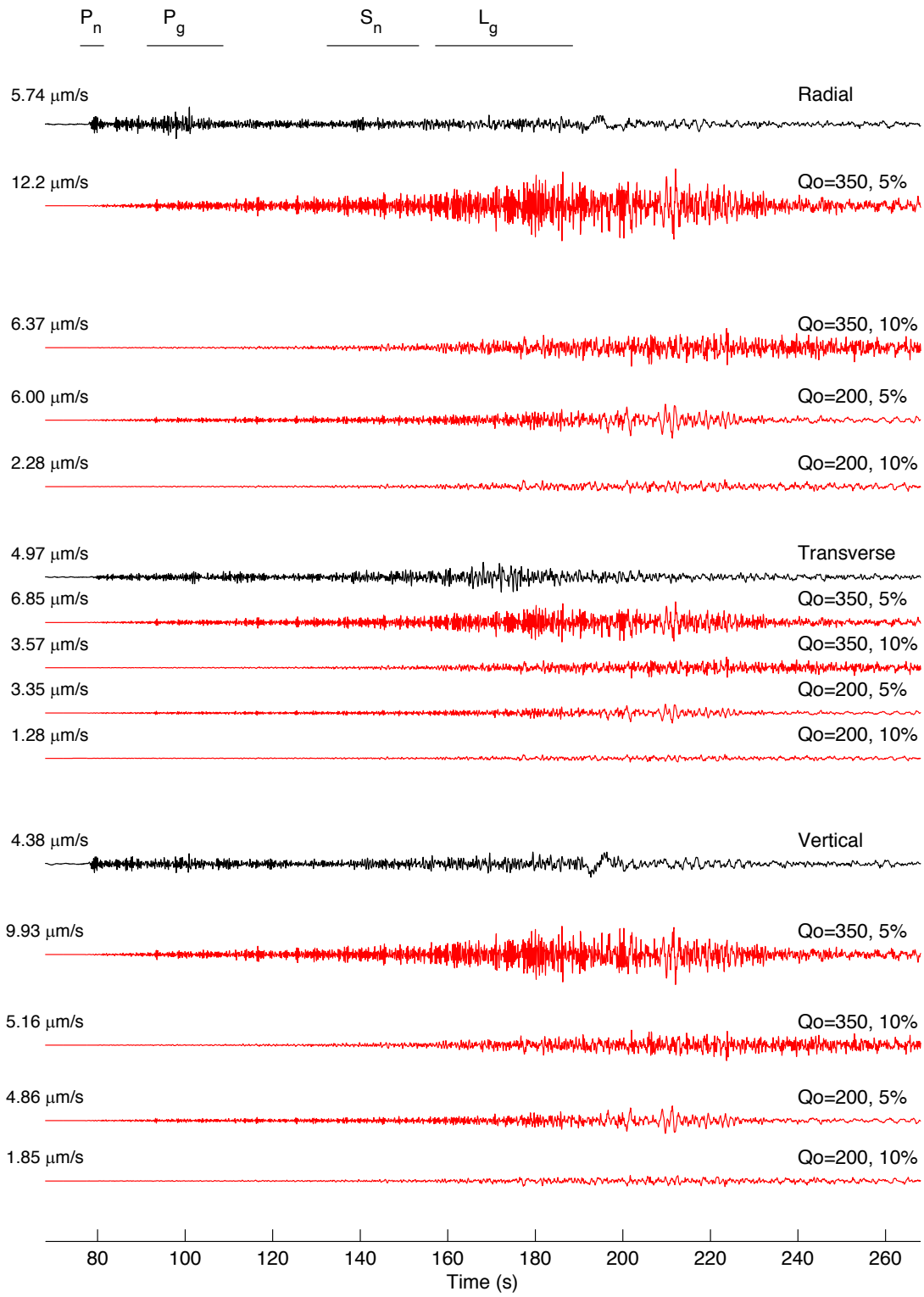

Figure A3. Comparison of observed (black) and synthetic waveforms at TJN for the SALSA3D model with Models 2-5 (Table 1).

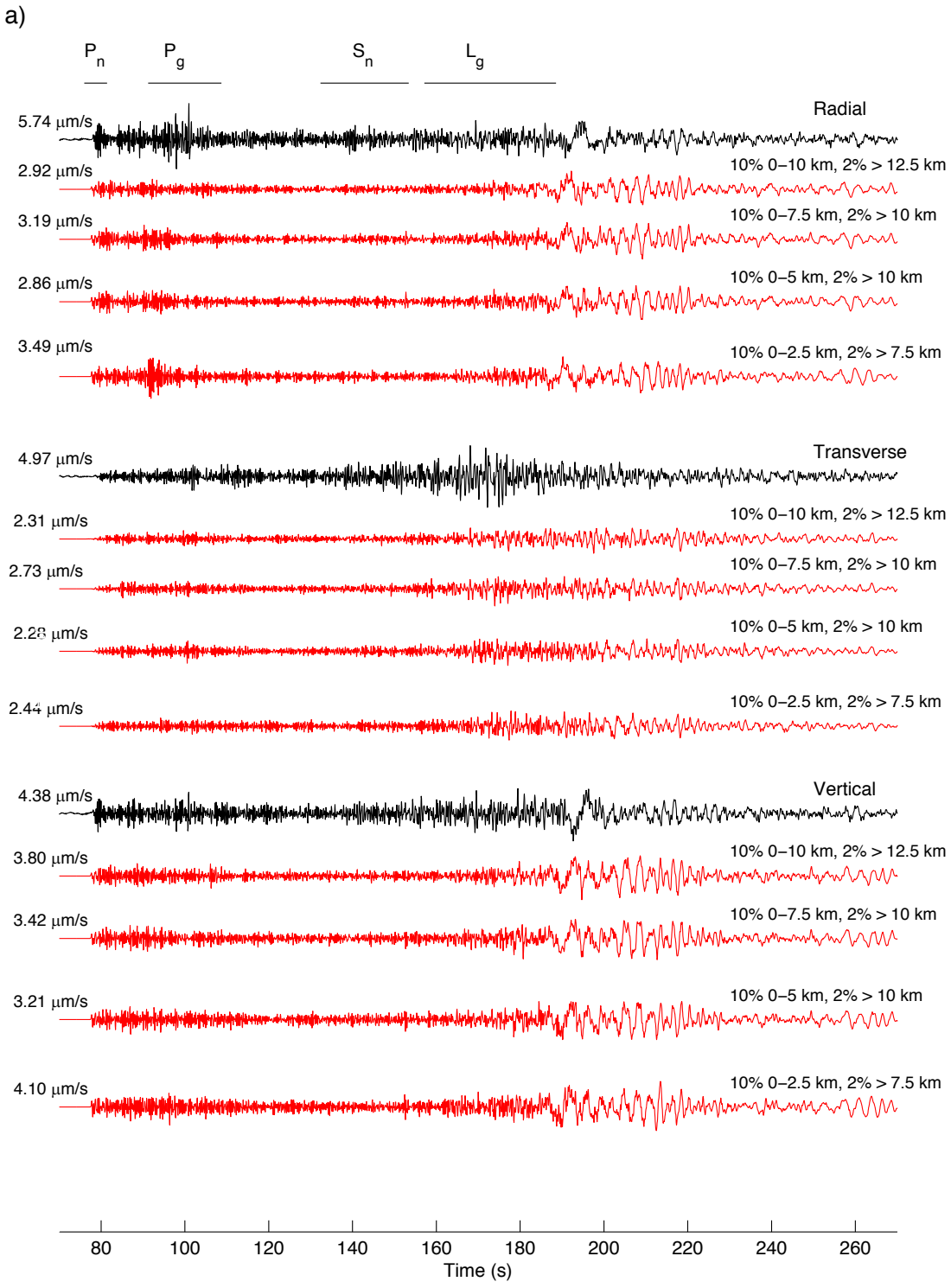

Figure A4. (a) Comparison of observed (black) and synthetic (red) waveforms at TJN for Models 6-9 (Table 1). ***The gradient models are all characterized by s = 10% from the surface to a depth of d1 km, s = 2% below a depth of d2 km, and a linear gradient in between. The values of d1 and d2 are listed by the synthetics.*** **(b) Comparison in the frequency domain for Model 6 (Table 1).**

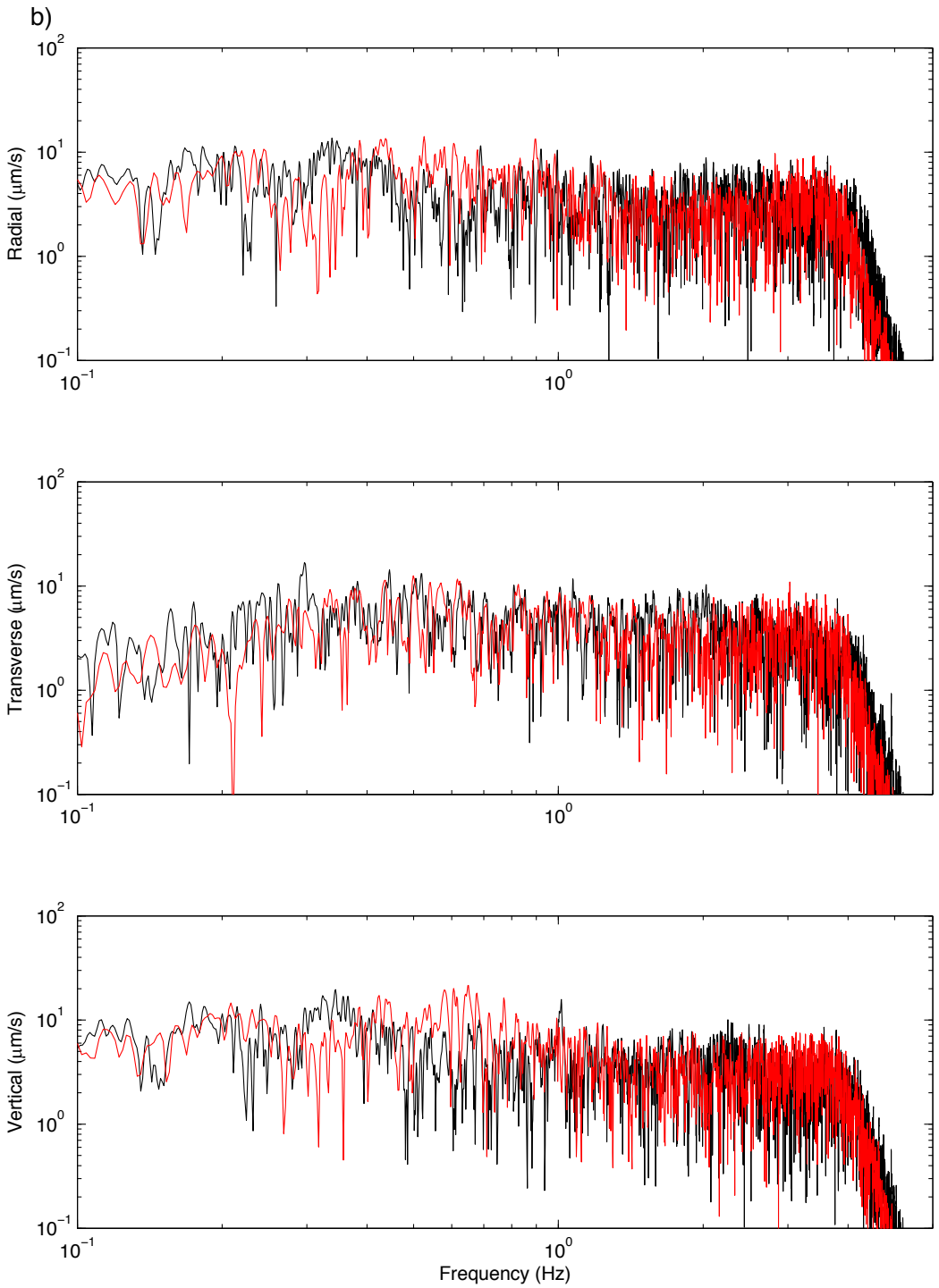

Figure A4 (continued). (a) Comparison of observed (black) and synthetic (red) waveforms at TJN for Models 6-9 (Table 1). ***The gradient models are all characterized by σ = 10% from the surface to a depth of d_1 km, σ = 2% below a depth of d_2 km, and a linear gradient in between. The values of d_1 and d_2 are listed by the synthetics.*** **(b) Comparison in the frequency domain for Model 6 (Table 1).**

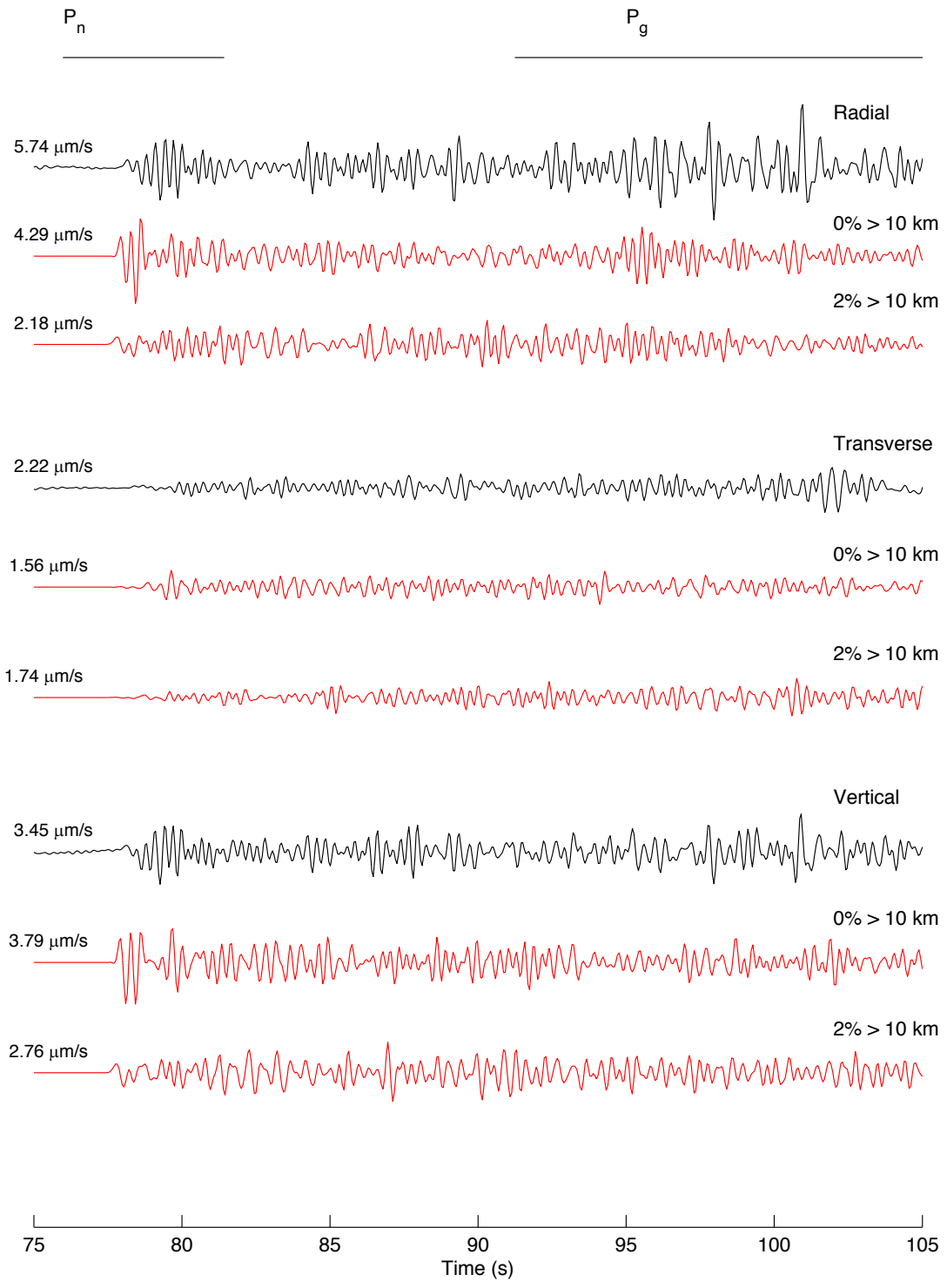

Figure A5. Zoom of the time domain comparison for TJN using Models 7 and 7a (Table 1). ***Peak velocities listed refer to the time interval shown.***

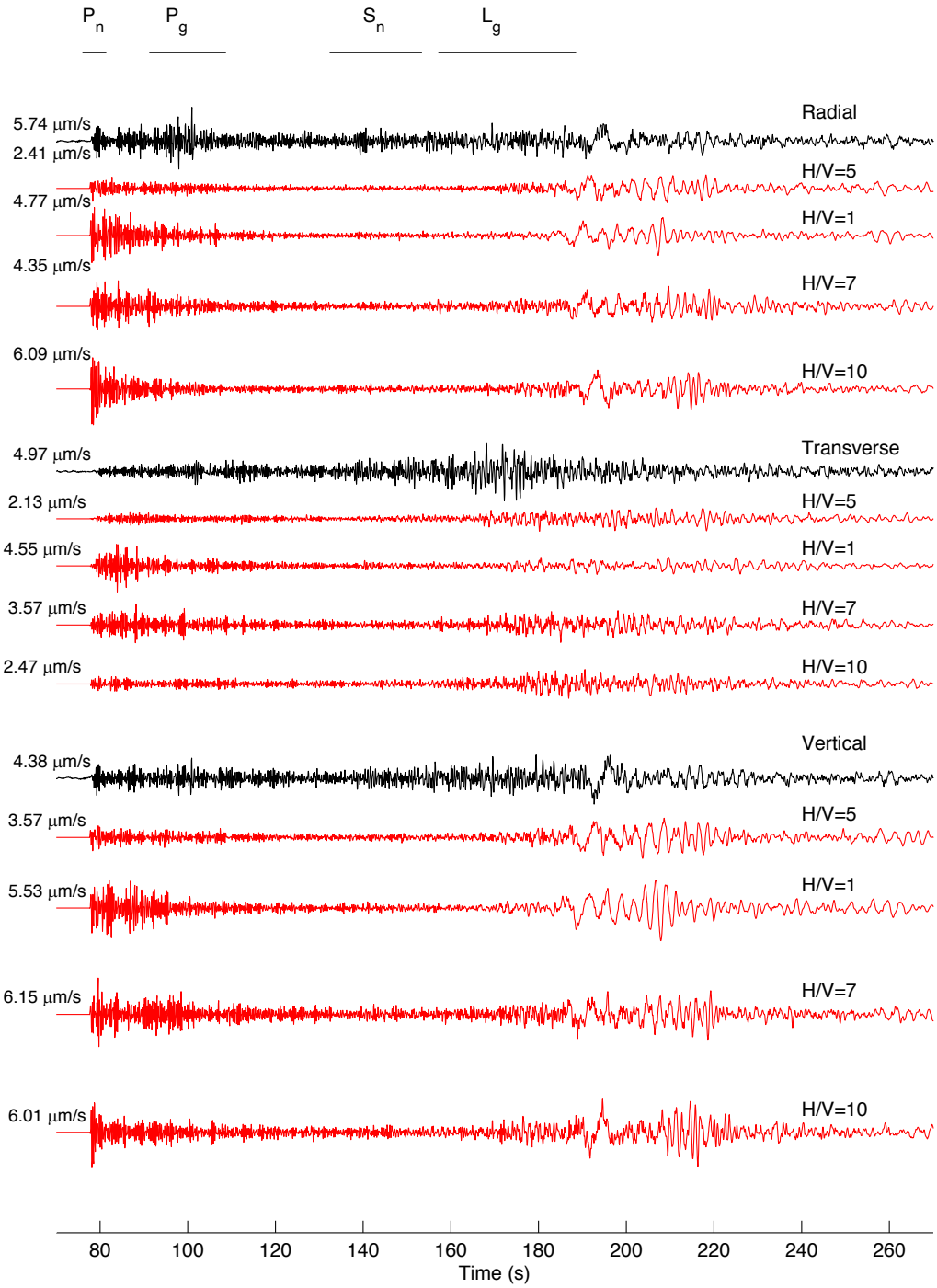

Figure A6. Comparison at TJN of the scattering effects from anisotropy in the small-scale heterogeneities, quantified by the ratio of horizontal-to-vertical dimensions of the velocity and density perturbations (H/V). ***Results for H/V=1, 5, 7, and 10 (Models 10, 6, 11 and 12, Table 1) are shown.***

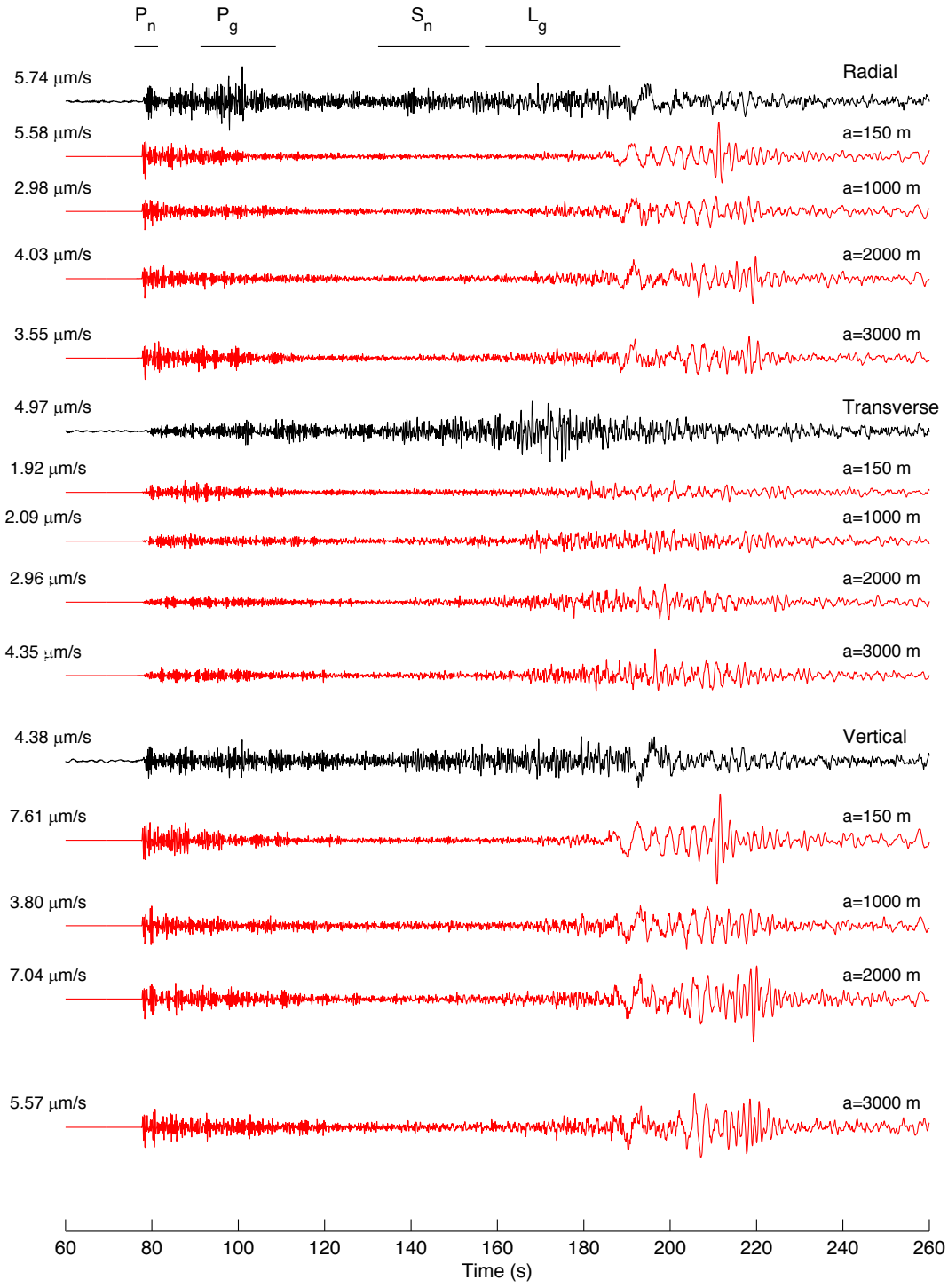

Figure A7. Comparison at TJN of the scattering effects from different correlation length in the distribution of small scale heterogeneities (150 m, 1,000 m, 2,000 m, and 3,000 m) as defined by Models 13, 6a, 14 and 15 (Table 1).

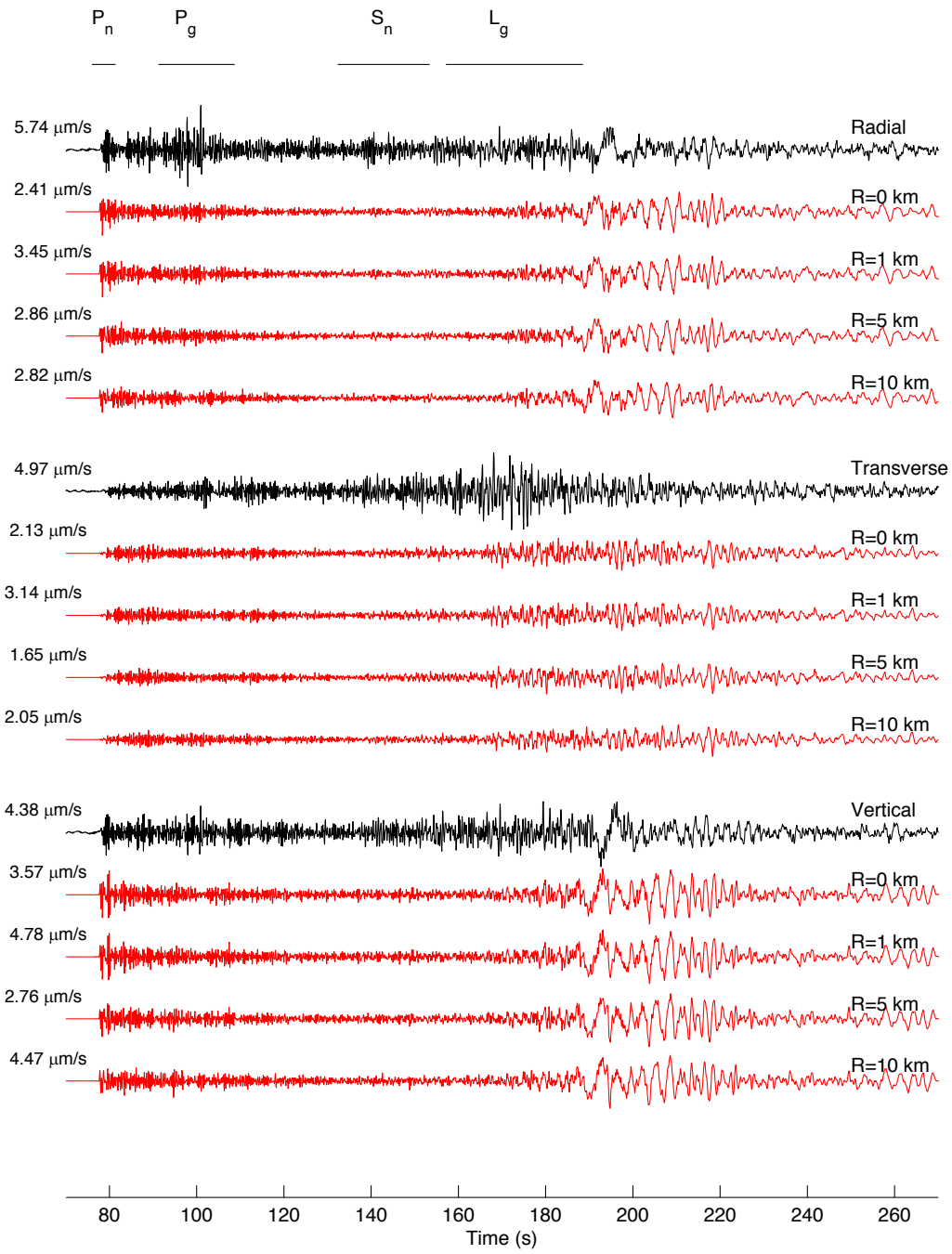

Figure A8. Significance of near-source scattering effects from small-scale heterogeneities at TJN. ***The small-scale heterogeneities (Model 6, Table 1) have been removed within radii (R) of 0-10 km from source, listed by the synthetics.***

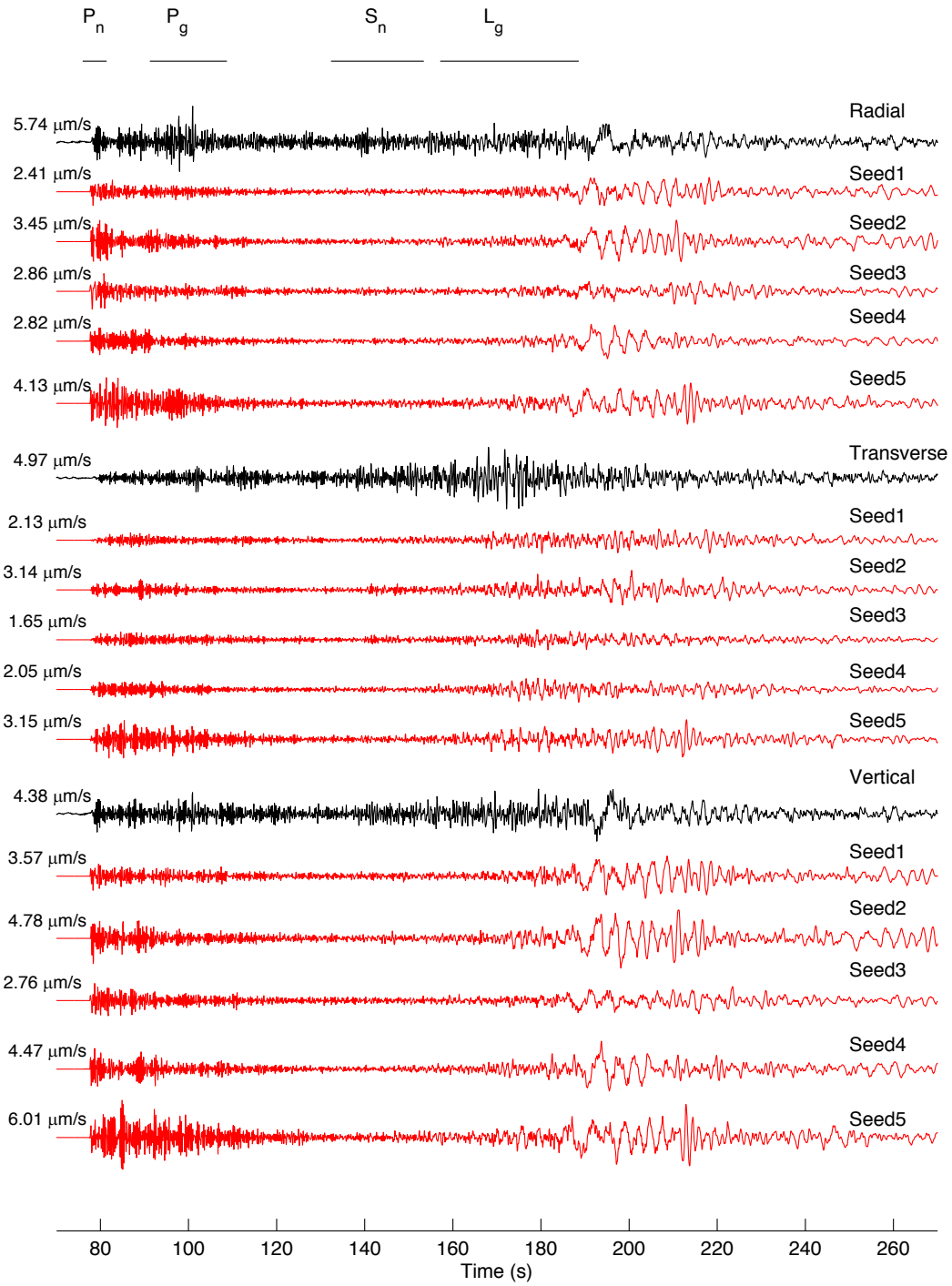

Figure A9. Comparison of data to synthetics generated from a 5-realization ensemble of statistical models of small-scale heterogeneities with different seed numbers at TJN. ***All simulations use the Q(f), H, a, H/V and σ of Models 16-20 (Table 1).***

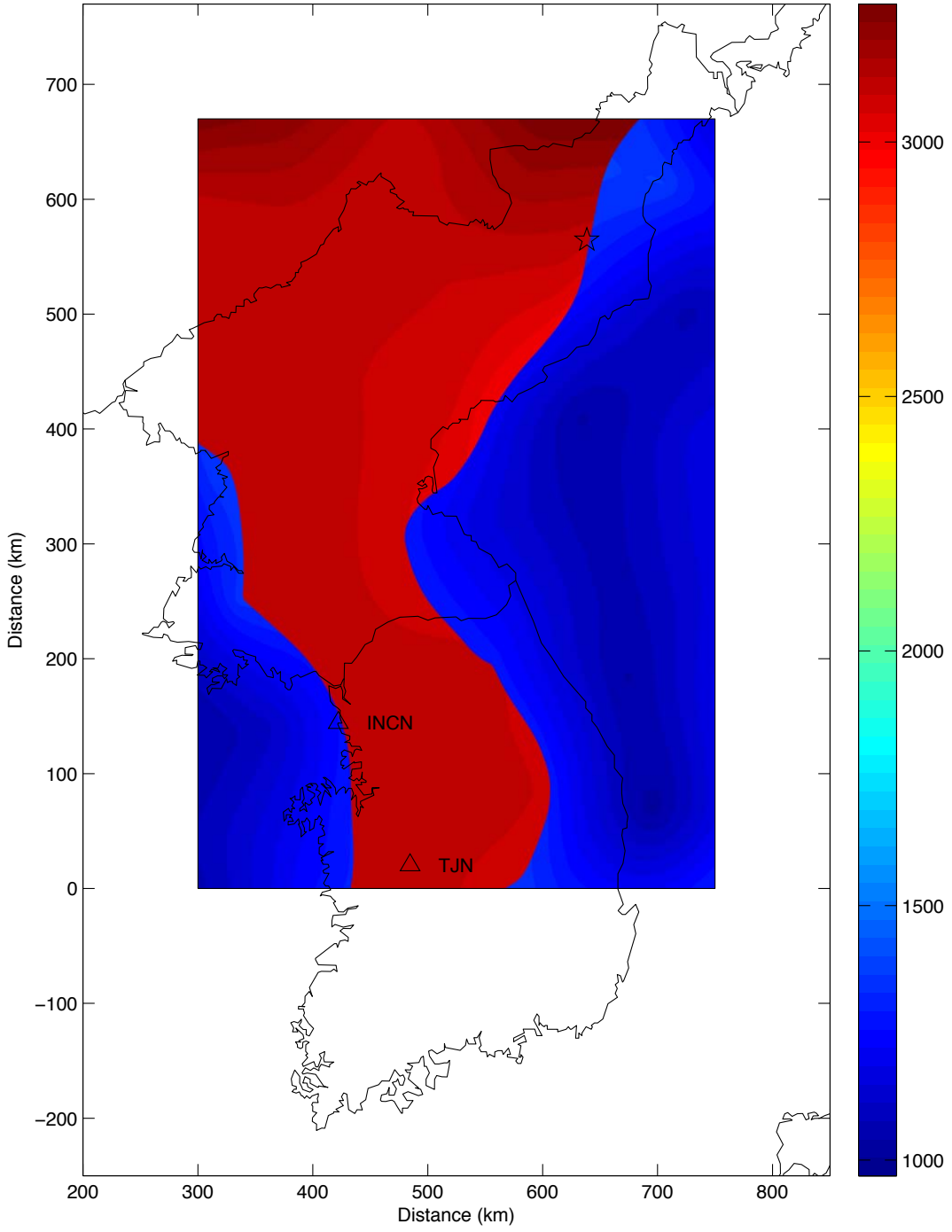

Figure A10. V_s (m/s) at the surface (z=0 km). ***The star denotes the source location for the May 25 2009 North Korea nuclear test. Two stations (INCN, TJN) in South Korea with instrument-corrected records available used in this study are shown by triangles.***

Appendix B

The next steps in the project includes applying the P/S ratio discrimination method to the high-frequency deterministic synthetics generated in this study. The ratio of P and S waves from seismic records has been shown to be an indicator of whether the source was an explosion or an earthquake. The deterministic simulations carried for the North Korea Nuclear Tests provide a good 'dataset' to test this method for synthetics, not only at the locations of the data records, but also at sites between the source and stations. However, due to the stochastic nature of the small-scale heterogeneities, where the statistics rather than the actual positions of the perturbations is constrained, it is necessary to use an ensemble of simulations for this test.

We will continue to improve the waveform fits at INCN and TJN searching for constraints for the small-scale crustal and mantle heterogeneities. We will include comparison of synthetics to data at additional stations, including KSI in South Korea, and stations from the Dongbei array in China.

We have started preparing simulations using a new FD-DM code with the water layer included, to explore effects on the fits at stations in South Korea for NKNTS sources. Toward this goal we will sample the top ~0-4 km of the model with a grid spacing of 33.33 m, 1/3 x the current spacing of 100 m. This will allow us to include the actual properties of the ocean (V_p~1,500 m/s, V_s=0 km/s, and ρ~1,000 kg/m^3).

We will start assembling a crustal and mantle model that extends from the Korean Peninsula to Japan, and perform initial simulations (up to 2 Hz including the ocean layer), testing whether the leakage of particularly L_g waves can be explained by the oceanic crust, in concert with the ocean water. Seismic data from Japanese stations will be included for comparison with the synthetics.

Initial tests with a hybrid deterministic-stochastic method (Olsen and Takedatsu, 2015) have been carried for the 2009 North Korean nuclear explosion recorded at INCN and TJN. The justification for this project is that the computational cost of such hybrid method is considerably less than the fully deterministic simulations carried out in this study. However, we have encountered numerical problems calculating the stochastic scattering function for the regional distances, where the method has not been applied before. We will continue to explore the method in the next year.

DISTRIBUTION LIST

DTIC/OCP
8725 John J. Kingman Rd, Suite 0944
Ft Belvoir, VA 22060-6218 1 cy

AFRL/RVIL
Kirtland AFB, NM 87117-5776 1 cy

Official Record Copy
AFRL/RVBYE/Dr. Frederick Schult 1 cy